Controls of Dynamic and Static Stress Changes and Aseismic Slip on Delayed Earthquake Triggering in Rate-and-State Simulations of the 2019 Ridgecrest Earthquake Sequence

Jeena Yun[1], Alice-Agnes Gabriel[1,2], Dave A. May[1], and Yuri Fialko[1]

[1]Scripps Institution of Oceanography, University of California San Diego, La Jolla, CA, USA
[2]Department of Earth and Environmental Sciences, Ludwig-Maximilians Universität München, Munich, Germany

Key Points:

- Simulations of stress perturbation due to the M_w 5.4 foreshock predict a clock advance of the mainshock of several hours.
- Instantaneous triggering does not occur unless stress perturbation is a large fraction of strength excess during quasi-static nucleation.
- The sign of stress perturbation in areas of accelerating slip controls the advance versus delay of the mainshock.

Corresponding author: Jeena Yun, `j4yun@ucsd.edu`

Abstract

Dynamic earthquake triggering often involves a time delay relative to the peak stress perturbation. In this study, we investigate the physical mechanisms responsible for delayed triggering. We compute detailed spatiotemporal changes in dynamic and static Coulomb stresses at the 2019 M_w 7.1 Ridgecrest mainshock hypocenter, induced by the M_w 5.4 foreshock, using 3D dynamic rupture models. The computed stress changes are used to perturb 2D quasi-dynamic models of seismic cycles on the mainshock fault governed by rate-and-state friction. We explore multiple scenarios with varying hypocenter depths, perturbation amplitudes and timing, and different evolution laws (aging, slip, and stress-dependent). Most of the perturbed cycle models show a mainshock clock advance of several hours. Instantaneous triggering occurs only if the peak stress perturbation is comparable to the strength excess during quasi-static nucleation. While both aging and slip laws yield similar clock advances, the stress-dependent aging law results in a systematically smaller clock advance. The sign of the stress perturbation in regions of accelerating slip controls whether the mainshock is advanced or delayed. In these models, mainshocks can be triggered even when static stress changes do not favor rupture at the future mainshock hypocenter, due to stress transfer from the foreshock sequence. Our results suggest that the Ridgecrest mainshock fault was already on the verge of runaway rupture and that both foreshocks and aseismic deformation may have contributed to earthquake triggering.

Plain Language Summary

Earthquakes can be triggered by stress changes induced by seismic waves from other earthquakes. These triggered events often exhibit a delay relative to the arrival time of the seismic waves. For example, the 2019 M_w 7.1 Ridgecrest, CA, mainshock occurred several hours after a nearby M_w 5.4 foreshock. The physical mechanism behind such delayed triggering remains unclear. In this study, we use computer simulations to explore the physical mechanisms responsible for delayed triggering. We compute detailed time-dependent stress changes at the Ridgecrest mainshock hypocenter caused by the M_w 5.4 foreshock and compare the timing of the mainshock in models with and without the stress perturbation, for different scenarios. Our results show that in most cases the perturbed mainshock occurs several hours earlier than it would without the perturbation. The clock advancement or delay depends on whether the stress change in regions of accelerating fault slip favors rupture. Even when stress changes at the future mainshock hypocenter do not favor rupture, stress transfer from the foreshock sequence can still trigger mainshocks. Our findings emphasize the important role of foreshock sequences and aseismic deformation in earthquake triggering.

1 Introduction

Some earthquakes may be encouraged by other earthquakes, a phenomenon called earthquake triggering (e.g., Freed, 2005; Hill & Prejean, 2015; Stein, 1999). Earthquake triggering has been documented using seismic and geodetic observations at various distances from the source, both in the near-field (within one or two fault lengths; e.g., Bosl & Nur, 2002; Hudnut et al., 1989; King et al., 1994; Parsons & Dreger, 2000) and far-fields (e.g., DeSalvio & Fan, 2023; Gomberg, 1996; Gomberg et al., 2001; Hill et al., 1993). Earthquake triggering has also been observed in laboratory experiments (e.g., Dong et al., 2022; Farain & Bonn, 2024; Y. Jin et al., 2021). One of the widely used frameworks to explain earthquake triggering considers changes in Coulomb failure stress (ΔCFS; Caskey & Wesnousky, 1997; Harris & Simpson, 1992; King et al., 1994). Slip on a fault can permanently alter the stress field, either promoting or inhibiting failure on surrounding faults. The static ΔCFS measures the relative contribution of permanent changes in shear stress and effective normal stress on a given 'receiver' fault. The magnitude and sign of ΔCFS indicate whether a fault is moved closer to failure. A region with positive static ΔCFS is considered to have an elevated likelihood of failure and is often well correlated with an increased rate of aftershocks, although there are notable exceptions (e.g., Hardebeck & Harris, 2022).

However, not all earthquakes appear to be triggered by static ΔCFS . Some presumably triggered earthquakes occur in regions with negative ΔCFS (stress shadow; Felzer & Brodsky, 2005) and at considerable distances from the causal earthquakes (e.g., Gomberg, 1996). The magnitude of static stress changes decreases rapidly with distance, becoming negligible at teleseismic distances (Árnadóttir et al., 2004; Gomberg et al., 2001). The concept of dynamic triggering considers changes in stress and/or strength due to passing seismic waves, which can produce an order of magnitude higher ΔCFS compared to static stress changes (Felzer & Brodsky, 2006; Kilb et al., 2000). Dynamic triggering may possibly explain the asymmetry in aftershock distributions due to rupture directivity (Kilb et al., 2000) and the occurrence of aftershocks within static stress shadows (Hardebeck & Harris, 2022). Additionally, dynamically triggered earthquakes are sometimes associated with geothermal fields or volcanic regions (e.g., Brodsky & Prejean, 2005), suggesting an important role of geothermal fluids interacting with faults.

While some dynamically triggered earthquakes occur at the time of the largest stress perturbation during the passage of seismic waves, a time delay between the largest perturbation and triggered earthquakes is frequently observed (e.g., Belardinelli et al., 1999; DeSalvio & Fan, 2023; Dong et al., 2022; Guo et al., 2024; Shelly et al., 2011). For example, the July 2019 M_w 7.1 Ridgecrest earthquake was preceded by multiple foreshocks, including the two largest events of M_w 6.4 and M_w 5.4 (Jia et al., 2020; Meng & Fan, 2021; Ross et al., 2019). The M_w 5.4 foreshock occurred only 16.2 hours before the mainshock, and the hypocenters of the two earthquakes were separated by only about 3 km. Previous studies showed that the nucleation site of the M_w 7.1 Ridgecrest mainshock likely experienced significant dynamic stress changes of several MPa (e.g., Z. Jin & Fialko, 2020; Taufiqurrahman et al., 2023). Another example is the February 2023 Kahramanmaraş, Turkey M_w 7.8-7.7 earthquake doublet, which exhibited a time difference of about 9 hours between the two earthquakes, with a large dynamic stress perturbation on the M_w 7.7 earthquake fault plane induced by the M_w 7.8 earthquake (Gabriel et al., 2023; Jia et al., 2023). Given the spatiotemporal proximity of the causal and triggered large earthquakes, it is important to understand why apparently large stress perturbations fail to instantaneously trigger faults that are presumably already on the verge of runaway rupture and what factors control delayed triggering.

Several hypotheses have been proposed to explain the observed time delay in dynamic earthquake triggering, including changes in frictional contacts (Parsons, 2005), aseismic slip triggered by dynamic stresses (Árnadóttir et al., 2004; Shelly et al., 2011), variations in pore pressure or fluid diffusion (Elkhoury et al., 2006; Gomberg et al., 2001), granular flow (Farain & Bonn, 2024; Johnson & Jia, 2005), and subcritical crack growth (Atkinson, 1984). Recently, Dong et al. (2022) observed delayed dynamic triggering in laboratory experiments. They infer a slow rupture phase and an increased critical slip distance near the P-wave perturbation, indicating a contribution of aseismic slip and changes in frictional contacts to delayed dynamic triggering.

Insights into the mechanics of earthquake triggering can be obtained from numerical modeling. Rate-and-state friction is a widely adopted constitutive law that describes the non-linear response of rock friction as a function of slip velocity and the state of the interface (Dieterich, 1979; Ruina, 1983). Single-degree-of-freedom spring slider models have provided useful insights into the sensitivity of the nucleation time in response to static or dynamic stress perturbations (Belardinelli et al., 2003; Dieterich, 1994; Gomberg et al., 1997; Perfettini et al., 2001; Pranger et al., 2022). More complex rate-and-state models incorporating multiple earthquake sequences (i.e., seismic cycle models) have enhanced the understanding of the effects of external stress perturbations on the temporal evolution of fast and slow slip instabilities (Gallovič, 2008; Kostka & Gallovič, 2016; Li & Gabriel, 2024; Luo & Liu, 2019; Perfettini et al., 2003a, 2003b; Tymofyeyeva et al., 2019; Wei et al., 2018) and changes in seismicity rates (Ader et al., 2014; Kaneko & Lapusta, 2008).

Despite considerable progress, many aspects of the physical mechanisms underlying earthquake triggering and delay remain unresolved. While far-field triggering is most likely dynamic in nature, distinguishing between the effects of static and dynamic triggering in the near-field is challenging. In the near-field, van der Elst and Brodsky (2010) estimated that dynamic strain accounts for the occurrence of 15% - 60% of magnitude 3 - 5.5 earthquakes, and Hardebeck and Harris (2022) estimated that $\sim 34\%$ of all aftershocks are driven by dynamic stress changes. However, these studies relied on approximate estimates of dynamic strain to quantify the effects of dynamic triggering. Although some previous studies have explored the individual effects of static (Dublanchet et al., 2013; Kaneko & Lapusta, 2008; Perfettini et al., 2003a) and dynamic (Ader et al., 2014; Perfettini et al., 2001, 2003b) stress changes, they have rarely considered the combined static and dynamic effects that natural faults are likely to experience.

Also, existing models of dynamic triggering typically rely on simplified stress histories to estimate the triggering response. For example, dynamic stress perturbations are often modeled as a single pulse or harmonic function (Ader et al., 2014; Gomberg et al., 1997; Luo & Liu, 2019; Perfettini et al., 2003b; Tymofyeyeva et al., 2019). A notable exception is Wei et al. (2018), who computed a detailed time series of ΔCFS inferred from a kinematic slip model, but neglected variations of ΔCFS with depth. While these simplified stress histories might be appropriate approximations for far-field triggering or near-surface processes, they fall short of capturing the complexities of near-field triggering mechanics. A comprehensive understanding of near-field triggering requires considering the detailed history of stress perturbation throughout the full seismogenic depth range.

The emergence of earthquake dynamic rupture and seismic cycle simulations that efficiently utilize high-performance computing (HPC) provides new opportunities to address existing knowledge gaps (e.g., Taufiqurrahman et al., 2023; Uphoff et al., 2023). High-accuracy 3D dynamic rupture simulations enable the computation of realistic histories of seismic stress perturbations, allowing the exploration of the combined contributions of static and dynamic stress changes. Similarly, HPC-empowered seismic cycle simulations can incorporate more realistic parameters that are closer to those observed in laboratory experiments and allow extensive exploration of the parameter space. Additionally, the increased computational capabilities facilitate volume-discretized methods (Erickson & Dunham, 2014; Liu et al., 2020; Pranger, 2020; Thakur et al., 2020; Uphoff et al., 2023), which can require high computational costs in terms of both storage and time-to-solution.

In this study, we investigate the physical factors and processes governing potential triggering relationships between the 2019 Ridgecrest M_w 5.4 foreshock and the M_w 7.1 mainshock. We record detailed spatiotemporal stress changes on the mainshock fault plane caused by the M_w 5.4 foreshock, considering a range of fault geometries and varying moment release rates using 3D dynamic rupture simulations (sections 2.1 and 3.1). We then perform a suite of quasi-dynamic seismic cycle simulations on a 2D vertical strike-slip fault representing the mainshock fault (sections 2.2 and 3.2). These cycle models are subsequently perturbed using stress perturbations calculated from the dynamic rupture model (Section 2.3). We extensively explore the change in timing of the mainshock (i.e., mainshock 'clock change') across different stress perturbation models, target mainshock depths, times intervals between perturbation and mainshock, amplitudes of stress perturbations, and state variable evolution laws (sections 3.3 and 3.4). We compare the correlation of the mainshock clock change with various physical factors, such as peak slip rate, static ΔCFS, and peak dynamic ΔCFS, to identify the controlling mechanisms behind the mainshock clock change. We find that the spatial distribution of depth-dependent static ΔCFS and aseismic deformation significantly affects the mainshock clock change (Section 4.3). This work proposes a novel framework for evaluating the combined effect of static and dynamic stress changes on near-field triggering and suggests a deterministic approach to estimating triggering potential. Additionally, we highlight the contributions of static stress change and background deformation in earthquake triggering and advocate for an integrative approach to assessing triggering potential.

2 Methods

2.1 Dynamic Rupture Simulations

We compute the coseismic spatiotemporal evolution of stress changes near the mainshock hypocenter location caused by the foreshock using 3D dynamic rupture simulations. To this end, we use the open-source dynamic rupture and seismic wave propagation simulation software *SeisSol* (Dumbser & Käser, 2006; Pelties et al., 2014), which is optimized for HPC infrastructure (Heinecke et al., 2014; Krenz et al., 2021; Uphoff et al., 2017) and has been applied to model rupture dynamics in various tectonic contexts (e.g., Biemiller et al., 2022; Ulrich et al., 2019). Our simulations include both the foreshock and mainshock faults within a 3D domain (Fig. 1a). In this model setup, the mainshock fault plane serves as the receiver plane, recording the dynamic and static stresses induced by the foreshock.

The foreshock rupture plane is modeled as a square fault with dimensions of 3 km by 3 km, centered at a depth of 7 km (USGS, 2017). We consider two dip angles, vertical and NW70° dip (USGS, 2017), to account for possible uncertainties in the fault dip estimation. To nucleate the earthquake, we prescribe a frictionally weak circular patch with a radius of 250 m at the center of the foreshock rupture plane.

The receiver mainshock fault extends from the free surface to a depth of 24 km, with a width of 3 km, and is centered at the M_w 7.1 mainshock epicenter location (USGS, 2017). We model scenarios using four different mainshock fault strikes (320°, 330°, 340°, and 350°) to cover a range of the average strike angles obtained from finite fault inversions of the M_w 7.1 mainshock (320°; Z. Jin & Fialko, 2020; Jia et al., 2020) and focal mechanisms (340°; SCEDC, 2013; Z. Jin & Fialko, 2020). Allowing for variations in the strike and dip of either fault accounts for uncertainties in the relative geometries of the two faults. Since we use eight different combinations of mainshock fault strikes and foreshock fault dips, the minimum distance between the two faults varies between 1303 m and 116 m. For models with a dipping foreshock fault, the horizontal extent of the mainshock fault is slightly reduced by 20 m (330°) or 500 m (320°) to prevent the two faults from intersecting. However, this variability in horizontal extent does not affect the stress change estimates, as we focus on the stress changes along a profile beneath the mainshock epicenter.

We embed both faults in a 3D velocity model (CVMS4.26.M01; E.-J. Lee et al., 2014; Small et al., 2017, 2022). We use a stress-free boundary condition for the flat free surface (at zero depth) and absorbing boundary conditions for all remaining model boundaries. The spatial resolution of dynamic rupture simulations must resolve the width of the process zone (Day et al., 2005; Ramos et al., 2022). On-fault, we use a uniform element size of 25 m for the foreshock. This resolution ensures accurately resolving the median cohesive zone width of 212.59 m measured on the foreshock fault (Wollherr et al., 2018). For the mainshock fault, we use an element size of 80 m. This model resolves the seismic wavefield up to frequencies of 6.9 Hz between the two faults. Away from the fault, we adaptively coarsen the unstructured tetrahedral mesh to element sizes of up to 1.5 km at $\sim$ 50 m away from both faults. The meshes used in this study contain 1.8

to 2.3 million elements and require ∼500 CPU hours on average on the supercomputer SuperMUC-NG for each 15-second simulation.

All dynamic rupture model parameters used in this study are summarized in Table 1. We use a linear slip-weakening friction law (Andrews, 1976; Ida, 1972; Palmer & Rice, 1973) where the fault strength τ_s is defined as

$$\tau_s = C_0 + \sigma_n \left(f_s - \frac{f_s - f_d}{D_{LSW}} \min(S, D_{LSW}) \right), \tag{1}$$

with the frictional cohesion C_0, the effective normal stress σ_n, the static and dynamic friction f_s and f_d, respectively, and the slip-weakening distance for the linear slip-weakening law D_{LSW}. We vary the combination of dynamic friction f_d and critical distance D_{LSW} to obtain models with different rupture characteristics (Table 1).

We assign a Cartesian initial stress tensor $\boldsymbol{\sigma}$ for the entire domain (Table 1). As a result, the initial normal and shear stresses on each fault vary depending on its orientation. For the foreshock fault, which is contained within the $xz-$plane, the initial normal stress is $\sigma_n^0 = \boldsymbol{\sigma}_{yy}$, and the initial shear stress $\tau_0 = \boldsymbol{\sigma}_{xy}$. The prestress level and the frictional fault strength can be characterized by the seismic parameter or relative strength parameter S (Andrews, 1976), which represents the ratio of the frictional strength excess to the maximum possible dynamic stress drop,

$$S = \frac{f_s \sigma_n^0 - \tau_0}{\tau_0 - f_d \sigma_n^0}, \tag{2}$$

where $f_s\sigma_n^0$ and $f_d\sigma_n^0$ are the static and dynamic strength, respectively. Smaller static and dynamic friction coefficients are assigned within the nucleation patch, resulting in an S ratio of -0.56, which gradually increases outside the patch towards the fault boundary (Fig. 1b).

From the stress changes recorded on the mainshock fault plane, we compute the time evolution of ΔCFS, which includes both static and dynamic stress changes, as follows:

$$\Delta\text{CFS}(z,t) = \hat{\tau}(z,t) - f\hat{\sigma}_n(z,t) \tag{3}$$

where z is depth, $t \in [0, 15]$ is time (in seconds), $f = 0.4$ is the friction coefficient, and $\hat{\sigma}_n$ and $\hat{\tau}$ are the normal and along-strike shear stress perturbations. The $\hat{\sigma}_n$ and $\hat{\tau}$ are stress changes with respect to the initial conditions. The peak dynamic ΔCFS at a certain depth then becomes $\max_t \Delta\text{CFS}(z,t)$, and the static ΔCFS at a certain depth is $\Delta\text{CFS}\ (z, 15 \text{ seconds})$. Since models with varying dip angles and moment rate functions yield slightly different total moments, we scale all stress estimates by a factor of $M_{5.4}/M_0$ where $M_{5.4}$ is the total moment expected for a magnitude 5.4 earthquake on our modeled foreshock fault, and M_0 is the total moment obtained from each model.

2.2 Seismic Cycle Simulations

2.2.1 Rate-and-State Friction Law

Sequences of earthquakes on the mainshock fault plane are modeled using seismic cycle simulations. These simulations assume frictional/material properties and background stress conditions, and forward compute the evolution of slip on the fault during interseismic, coseismic, and postseismic periods, based on rate-and-state friction laws. We use the open-source seismic cycle simulator *Tandem* (Uphoff et al., 2023) to simulate quasi-dynamic anti-plane motions on a 2D vertical strike-slip fault (Fig. 2a). *Tandem* is based on a symmetric interior penalty discontinuous Galerkin method and is optimized for high-performance computing. *Tandem* uses the regularized version of the rate-and-state friction formulation (Lapusta et al., 2000) where the friction $F(\|\boldsymbol{V}\|, \theta)$ is expressed as

$$F(\|\boldsymbol{V}\|, \theta) = a \sinh^{-1}\left[\frac{\|\boldsymbol{V}\|}{2V_0} \exp\left(\frac{f_0 + b\ln(V_0\theta/D_{RS})}{a}\right)\right], \tag{4}$$

where $\|\boldsymbol{V}\|$ is the Euclidean norm of the slip rate vector $\boldsymbol{V}$, θ is the state variable, a, b are the rate-and-state parameters for direct and evolution effect, respectively, D_{RS} is the characteristic state evolution distance, V_0 is the reference slip rate, and f_0 is the reference friction coefficient. All seismic cycle model parameters used in this study are summarized in Table 2.

The sign of $(a-b)$ determines the stability of the system. An increase in sliding velocity leads to a drop of static friction when $a-b<0$, promoting instability, which is referred to as velocity-weakening (VW) behavior. Conversely, static friction increases when $a-b>0$, suppressing instability, which is defined as velocity-strengthening (VS) behavior. In our models, we include shallow and deep VS regions surrounding a central VW zone, representing the 10-km-wide seismogenic zone (Fig. 2a). The rate-and-state fault is loaded from the bottom creeping zone and the far boundary with a constant velocity (V_{pl}) corresponding to the long-term fault slip rate. Most of our simulations are performed using $V_{pl} = 10^{-9}$ m/s, but we also performed several simulations with $V_{pl} = 3.2\times10^{-11}$ m/s, corresponding to the slip rate of the Ridgecrest fault (∼1 mm/yr; Amos et al., 2013).

In quasi-dynamic simulations, the inertial effect is approximated by a radiation damping term $\eta\boldsymbol{V}$ (Rice, 1993):

$$-\boldsymbol{\tau} = \sigma_n F(\|\boldsymbol{V}\|, \theta)\frac{\boldsymbol{V}}{\|\boldsymbol{V}\|} + \eta\boldsymbol{V}, \tag{5}$$

where $\eta = \mu/2c_s$ is half of the shear-wave impedance with shear modulus μ and shear-wave speed c_s, and $\boldsymbol{\tau}$ and σ_n are shear and normal stresses on the fault, respectively. Although quasi-dynamic models do not capture all details of full elastodynamic solutions, they produce qualitatively comparable slip patterns at considerably lower computational cost (Thomas et al., 2014). Also, Kroll et al. (2023) found similar characteristics of rupture jumping for quasi-dynamic and fully dynamic models in the near field. Since the dynamic wave propagation effect is well captured in the 3D dynamic rupture models (Section 2.1), the quasi-dynamic approximation is a reasonable choice for modeling earthquake sequences on the mainshock fault.

The shear and normal stresses are expressed as the sum of the background stress ($\boldsymbol{\tau}^0$ or σ_n^0) and the traction resolved on the fault from a stress tensor ($\boldsymbol{\sigma}$) at a given displacement ($\boldsymbol{u}$):

$$\boldsymbol{\tau} = \boldsymbol{\tau}^0 + \boldsymbol{B}\boldsymbol{\sigma}(\boldsymbol{u})\boldsymbol{n}, \tag{6}$$

$$\sigma_n = \max\left(0, \sigma_n^0 - \boldsymbol{n}\cdot\boldsymbol{\sigma}(\boldsymbol{u})\boldsymbol{n}\right), \tag{7}$$

where $\boldsymbol{B}$ is the fault basis function and $\boldsymbol{n}$ is the fault normal vector. In the anti-plane model setup, the shear stress has only the along-strike component, resulting in scalar functions $\tau(z,t)$ and $\tau^0(z)$.

We use adaptive time stepping handled by the software PETSc (Abhyankar et al., 2014; Amestoy et al., 2001, 2006; Balay et al., 1997, 2019) with a fourth-order embedded fifth-order Dormand-Prince scheme Runge-Kutta method.

2.2.2 State Variable Evolution Laws

The evolution of the state variable θ is governed by an ordinary differential equation:

$$\frac{d\theta}{dt} = G(\|\boldsymbol{V}\|, \theta). \tag{8}$$

The two most commonly used formulations for the state variable evolution are the aging law (Dieterich, 1979):

$$G(\|\boldsymbol{V}\|, \theta) = 1 - \frac{\|\boldsymbol{V}\|\theta}{D_{RS}} \qquad \text{(Aging Law)}, \tag{9}$$

and the slip law (Ruina, 1983):

$$G(\|\boldsymbol{V}\|,\theta) = -\frac{\|\boldsymbol{V}\|\theta}{D_{RS}} \ln\left(\frac{\|\boldsymbol{V}\|\theta}{D_{RS}}\right) \qquad \text{(Slip Law).} \tag{10}$$

The aging law effectively captures the time-dependent healing of the rock surface (e.g., Dieterich & Kilgore, 1994), while the slip law accurately models the evolution of friction in velocity stepping experiments with large velocity changes (e.g., Ampuero & Rubin, 2008). A detailed description of different model resolution requirements for each evolution law is provided in Supplementary Section S1.

Laboratory experiments with normal stress perturbation show an instantaneous change in rock strength when subjected to a sudden change in normal stress (e.g., Boettcher & Marone, 2004; Linker & Dieterich, 1992; Pignalberi et al., 2024). To account for the immediate response to external stress perturbations, a stress-dependent term can be added to the basic state evolution laws ($G(\|\boldsymbol{V}\|,\theta)$ from Eqs. (9) and (10)):

$$\frac{d\theta}{dt} = G(\|\boldsymbol{V}\|,\theta) - \alpha\frac{\theta}{b}\frac{\dot{\sigma}_n}{\sigma_n}, \tag{11}$$

where α is a scaling factor that can vary from 0 to the static friction coefficient (Boettcher & Marone, 2004; Wei et al., 2018), and $\dot{\sigma}_n$ is the time derivative of normal stress. We use $\alpha = 0.3$ (Boettcher & Marone, 2004; Richardson & Marone, 1999).

2.2.3 Fractal Heterogeneities

The hypocentral depth estimations of the Ridgecrest mainshock vary from 3 km to 8 km depending on the method and data used (Hauksson & Jones, 2020; Z. Jin & Fialko, 2020). To account for this uncertainty in the depth estimation, we seek models with earthquakes nucleating at various depths within the seismogenic zone. The variability in the hypocenter depth may spontaneously occur without heterogeneous model parameters in 3D models with multiple faults (Yin et al., 2023) or in fully dynamic models with a low rigidity layer surrounding the fault (Thakur et al., 2020). However, the earthquake nucleation in quasi-dynamic cycle models on a 2D fault with homogeneous parameters is often restricted to the edges of seismogenic zones (e.g., Cattania, 2019). In order to generate a variety of hypocenter depths in our simulations, we introduce heterogeneity to the model parameters.

We introduce band-limited self-affine fractal variations to the initial effective normal stress (σ_n^0), rate-and-state parameters ($a-b$), and the characteristic state evolution distance (D_{RS}). The self-affine fractal variation is inspired by the fractal fault roughness observed on natural faults (J.-J. Lee & Bruhn, 1996; Renard et al., 2006). Here, we emulate the effects of rough fault surfaces by incorporating fractal variation into the initial fault stress and strength parameters. Heterogeneity in frictional properties was considered in a number of previous studies (Galvez et al., 2020; Hillers et al., 2007; Jiang & Fialko, 2016; Luo & Ampuero, 2018). The 1D fractal distributions are characterized by the power spectral density $P(k)$ as follows (Andrews & Barall, 2011; Dunham et al., 2011):

$$P(k) \propto k^{-(2H+1)} \tag{12}$$

with the wavenumber k and the Hurst exponent H. The Hurst exponent $H = 1$ results in a self-similar fractal distribution, while $0 \leq H < 1$ produces a self-affine distribution. For natural faults, H is typically assumed to vary between 0.4 to 0.8 (Renard & Candela, 2017). We set $H = 0.7$ for all fractal profiles used in this study (Cattania & Segall, 2021). The fractal variation is limited between a minimum (λ_{min}) and maximum (λ_{max}) wavelengths. We explore a wide range of λ_{min} from 30 m (nucleation size) to 750 m and λ_{max} from 2.5 km to 10 km (W_S) to identify a pair of λ_{min} and λ_{max} that produces enough complexity in both rupture extent (e.g., emergence of both partial rupture and system-size rupture) and hypocenter depth (i.e., widely distributed nucleation locations within the seismogenic zone).

We use a Fourier transform method (Andrews & Barall, 2011; Shi & Day, 2013) to generate the fractal profile and take an amplitude-to-wavelength ratio of 10^{-2} to scale the root-mean-square amplitude of the profile (Dunham et al., 2011). All fractal variations are tapered outside the seismogenic zone by scaling their amplitude by the distance from the nearest VW depth point. The fractal amplitudes are then converted into variations of parameters by applying scaling factors that match the order of magnitude of each parameter. For example, the fractal effective normal stress profile is obtained by scaling the fractal height by $(\rho_c - \rho_w)g$ where $\rho_c = 2670$ kg/m^3 is density of crust, $\rho_w = 1000$ kg/m^3 is density of water, and $g = 9.8$ kg/m^3 is the acceleration due to gravity. Since the fractal heterogeneity has a mean of zero, the average value for each parameter (i.e., $\overline{\sigma_n^0}$, $\overline{a-b}$, and $\overline{D_{RS}}$) remains the same for both fractal (red solid lines in Figs. 2b-d) and non-fractal (grey dashed lines in Figs. 2b-d) distributions.

2.2.4 Event Detection and Classification

We implement an automated event detection and classification algorithm to systematically compare the event time and hypocenter locations across different models. A seismic event is identified when the peak slip rate along the fault exceeds a threshold of 0.2 m/s for more than 0.5 seconds at more than one of the evaluation points which are spaced every 200 m along the rate-and-state fault. An event is disregarded if the difference between the maximum and minimum peak slip rates during the event is less than 15% of the threshold velocity (0.2 m/s) to eliminate minor fluctuations in slip rate.

A 'system-size earthquake' is defined as an event that ruptures a length greater than 10 km (i.e., the entire seismogenic zone), while all other events are denoted 'partial rupture events' hereafter. A 'leading foreshock' is defined as the first partial rupture event in a sequence that eventually leads to a system-size earthquake.

2.3 Combining Dynamic Rupture and Seismic Cycle Simulations

To estimate the triggering response of the mainshock nucleation site to the stress transfer from the foreshock, we perturb the seismic cycle models (Section 2.2) using stress perturbations calculated from the dynamic rupture simulation (Section 2.1). The detailed approach is as follows (Fig. 3):

1. Run 3D dynamic rupture models rupturing the foreshock fault and record the normal ($\hat{\sigma_n}$) and shear stress ($\hat{\tau}$) perturbations across the (locked) mainshock fault beneath the mainshock epicenter (Section 2.1; Fig. 3b).
2. Run a 2D seismic cycle model and obtain N cycles using either the aging law (Eq. (9)) or the slip law (Eq. (10)). We refer to these models as 'unperturbed' reference models (black line in Fig. 3a).
3. Among the N cycles of the unperturbed seismic cycle model, choose one cycle with a system-size earthquake. The selected system-size earthquake will be called a 'target mainshock'. Identify the time of occurrence for the target mainshock, t_u.
4. Restart and run the cycling experiment from time $t = t_u - t_g$ where t_g is the time interval between the start of the perturbation (corresponding to the time of the M_w 5.4 foreshock) and the mainshock. Unless otherwise noted, t_g is set to 16.2 hours, the time interval between the M_w 5.4 foreshock and the M_w 7.1 mainshock in the 2019 Ridgecrest earthquake sequence (USGS, 2017). During this stage, the time-dependent normal ($\hat{\sigma}_n$) and shear ($\hat{\tau}$) stress changes on the mainshock fault simulated in the dynamic rupture simulations (Section 2.1) are added to those of the unperturbed seismic cycle model (τ & σ_n) at each time step, yielding the perturbed

normal stress (σ_n^p) and shear stress (τ^p):

$$\tau^p(z,t) = \tau(z,t) + \hat{\tau}(z,t)$$

$$\sigma_n^p(z,t) = \sigma_n(z,t) + \hat{\sigma}_n(z,t).$$

This phase will be denoted as the 'perturbation period', which lasts 15 seconds. During this stage, we use a fixed time step of 0.01 seconds to match the time interval of the dynamic rupture simulation outputs.

5. After the perturbation ends (i.e., $t > t_u - t_g + 15$ seconds) keep the static stress changes:

$$\tau^0(z) = \tau^0(z) + \hat{\tau}(z,t_f)$$

$$\sigma_n^0(z) = \sigma_n^0(z) + \hat{\sigma}_n(z,t_f),$$

where $t_f = t_u - t_g + 15$ seconds is the final time of the perturbation period. Continue running the seismic cycle simulation until a system-size earthquake occurs, and record the time of this event, t_p (blue line in Fig. 3a). This model is referred to as a 'perturbed' model.

6. Calculate the time difference between the system-size earthquakes with and without the perturbation: $\Delta t = t_u - t_p$. Δt is a measure for the triggering response. A positive Δt indicates that the perturbed system-size earthquake (mainshock) occurs earlier than in the unperturbed model, indicating a clock advance. A negative Δt indicates a mainshock clock delay.

Incorporating the stress-dependent aging law (combine Eq. (9) and Eq. (11)) requires a slight modification during the perturbation period (i.e., step 4 above):

1. Repeat steps 1 - 3 as outlined above.
2. During the perturbation period ($t \in [t_u - t_g, t_u - t_g + 15 \text{ seconds}]$), apply the stress-dependent aging law (Eq. (9) and Eq. (11)). The stressing rate during this perturbation ($\dot{\sigma}_n^p$) depends solely on the external stress perturbation ($\hat{\sigma}_n$):

$$\begin{aligned}\dot{\sigma}_n^p(z,t) &= \dot{\sigma}_n(z,t) + \dot{\hat{\sigma}}_n(z,t)\\ &= \dot{\sigma}_n^0(z) + \dot{\hat{\sigma}}_n(z,t)\\ &= \dot{\hat{\sigma}}_n(z,t)\,,\end{aligned}$$

since the background normal stress in the seismic cycle simulation (σ_n^0) remains constant over time (i.e., $\dot{\sigma}_n^0(z) = 0$). Then, Eq. (11) becomes:

$$\frac{d\theta}{dt} = G(\|\boldsymbol{V}\|,\theta) - \alpha\frac{\theta}{b}\frac{\dot{\sigma}_n^p}{\sigma_n^p} = G(\|\boldsymbol{V}\|,\theta) - \alpha\frac{\theta}{b}\frac{\dot{\hat{\sigma}}_n}{\sigma_n + \hat{\sigma}_n},$$

where $G(\|\boldsymbol{V}\|,\theta)$ follows Eq. (9). Aside from the state variable evolution law, everything else is the same as step 4 in the previously described procedure.

3. For $t > t_u - t_g + 15$ seconds, switch the state variable evolution law back to the aging law (Eq. (9)) and keep the constant static stress change. Repeat steps 5 - 6 in the previously described procedure to obtain Δt.

3 Results

3.1 Dynamic and Static Stress Change Estimation

The 3D dynamic rupture simulations well capture the dynamics of the M_w 5.4 foreshock along the mainshock fault. Figure 4 shows an example of the spatiotemporal evolution of the ΔCFS across the mainshock fault with 340° strike. The dynamic stress transfer mediated by body waves and reflections from the free surface are clearly observed.

The peak dynamic ΔCFS values fall between 0.4 MPa and 2 MPa (Fig. S1a), consistent with the previous estimate by Z. Jin and Fialko (2020) based on a point source approximation. The static ΔCFS values are generally on the order of kPa (Figs. S1c-d). The sign of the static ΔCFS changes from negative in the middle of the seismogenic zone (between 5 km and 10 km) to positive at smaller depths (< 5 km) and greater depths (> 10 km), likely reflecting the radiation pattern (Fig. 4).

The rupture characteristics of the M_w 5.4 foreshock mostly affect the arrival time and the amplitude of the peak dynamic ΔCFS, while having a negligible effect on the pattern of static ΔCFS (left vs. right columns of Fig. 4). We explore varying combinations of f_d and D_{LSW} to obtain two distinctive dynamic rupture characteristics that differ in their timing of the peak energy release (Fig. 1c): one set of models nucleates and releases all its energy immediately (denoted 'fast initiation' hereafter), while the others nucleate slowly, with pronounced runaway rupture initiating after 0.5 seconds (denoted 'slow initiation' hereafter). The slow initiation model features two episodes of moment release: one at the initial, prescribed time of rupture initiation and a second at the point of spontaneous runaway rupture. This resembles the two subevents with a 0.8 seconds time interval observed from the M_w 5.4 foreshock (Meng & Fan, 2021). The difference in moment release rate is well reflected in the spatiotemporal patterns of ΔCFS . Slow initiation models show delayed arrivals of the peak dynamic ΔCFS (Fig. 4) with reduced amplitudes (Fig. S1a) compared to the fast initiation models. The reduced amplitude is likely caused by the energy distribution to each subevent in the slow initiation models.

The mainshock fault strike systematically affects the amplitude of the peak dynamic ΔCFS and the static ΔCFS, while the foreshock fault dip affects the seismic radiation, altering the arrival time, depth, and amplitude. More northerly strike angles systematically decrease the amplitude of the peak dynamic ΔCFS and the static ΔCFS . Although the foreshock fault dip does not significantly affect the peak dynamic ΔCFS values, the dipping foreshock fault produces a stronger contrast between the positive and negative static ΔCFS values. The vertical foreshock fault produces near-symmetric wave propagation with respect to a depth of ~ 7 km, whereas the dipping foreshock fault shows asymmetric propagation. This apparent asymmetry is caused by the asymmetric arrival of the strong dynamic ΔCFS pulse due to the rotation of the radiation field in the dipping foreshock fault models, although the actual rupture speed is similar for various depths. The rotation of the radiation field also makes the depth of the peak dynamic ΔCFS smaller (except for the 350° strike).

Throughout the remainder of this study, we divide the stress perturbation models into four classes defined by the combination of the foreshock fault dip and the rupture characteristics: the vertical foreshock fault and the fast initiation model (VFI), the vertical foreshock fault and the slow initiation model (VSI), the dipping foreshock fault and the fast initiation model (DFI), and the dipping foreshock fault and the slow initiation model (DSI). Therefore, we have 16 dynamic rupture models in total, combining the four model classes with four mainshock strike angles.

3.2 Reference Seismic Cycle Models

We explore a range of heterogeneities to yield a reference seismic cycle model with realistic variability in both event size and hypocenter depth distribution. Using the aging law, we find that neither heterogeneity in any single parameter (Figs. 5a & S2) nor the presence of a low-rigidity fault zone alone is sufficient to introduce the desired complexity (Fig. S3; see Supplementary Section S2). Models with heterogeneity in any single parameter exhibit characteristic cycles and hypocenters located only at the periphery of the seismogenic zone, similar to results from models that do not assume any fractal heterogeneity (e.g., Lindsey & Fialko, 2016). This lack of complexity in earthquake cycles is consistent across all single-parameter heterogeneity models with varying fractal profiles (Fig. S2). We also tested models in which normal stress increases with depth with superimposed fractal heterogeneity (Fig. S2c), but the cycles remained repeatable, with nucleation limited to the lower edge of the seismogenic zone, where the critical nucleation size (L_∞, see Supplementary Section S1) becomes significantly smaller.

Introducing an $(a-b)$ profile with VS patches within the seismogenic VW region (Fig. 2c) gives rise to earthquakes that nucleate at various depths within the seismogenic zone, rather than only at its periphery (Fig. 5b-d). Earthquakes nucleate at the boundaries of VS patches, where the stressing rate is increased due to creep on VS patches. Combining this $(a-b)$ profile with heterogeneity in other model parameters introduces a greater diversity in the spectrum of ruptures. For example, heterogeneity in both stress and strength, along with a small $\overline{D_{RS}}$ value of 2 mm, produces slow slip events, partial ruptures, and system-size earthquakes (Fig. 5c). The hypocentral depths of the system-size events are well-distributed throughout the seismogenic zone. However, the sequence is still periodic, with a fixed nucleation depth for system-size earthquakes.

We confirm that the ratio of the width of the seismogenic zone to the critical nucleation size (i.e., W_S/L_∞) controls the system's complexity, including its periodicity (i.e., Barbot, 2019; Cattania, 2019). For instance, the two models in Figures 5c and 5d share the same set of parameters, except that the model in Figure 5d has a lower bulk rigidity ($\mu = 32$ GPa vs. $\mu = 20$ GPa), resulting in a smaller L_∞ and a higher value of W_S/L_∞. As expected, the model with a higher W_S/L_∞ value produces aperiodic sequences with a wide range of hypocenter depths and a diverse spectrum of ruptures.

We obtain the most complex model (Figs. 5d and 6a) by combining heterogeneity in all three parameters (red profiles in Figs. 2b-d) with a bulk rigidity of 20 GPa and $\overline{D_{RS}} = 2$ mm. In this model, system-size earthquakes are consistently preceded by a cascade of partial rupture events. This model has an average W_S/L_∞ of 86 with a maximum of 612 (note that we have a depth-varying W_S/L_∞ ratio due to the fractal distribution of parameters). We run this model for 5000 years of simulation time and use it as our reference model for subsequent simulations assuming aging law (denoted 'aging law reference model' hereafter). The non-repeating cycles and diverse distribution of hypocenter depths in this model allow exploration of the triggering response in earthquake cycles with diverse characteristics.

The aging law reference model also produces spontaneous deep and shallow slow slip events (SSEs; Beroza & Ide, 2011; Rousset et al., 2019; Wei et al., 2013) following system-size earthquakes or partial rupture events (Figs. 6a & S4). Deep SSEs occur after both a major partial rupture sequence and sequences that eventually lead to a system-size earthquake. The deep SSEs spatially coincide with a small VW patch embedded within the VS zone. This suggests that instability is initiated at the VW patch but fails to grow into a runaway seismic rupture due to the VS barriers located above and below. The recurrence time of the deep SSEs is generally shorter when preceded by a system-size earthquake (Fig. S4c), implying that slow slip transients occur more frequently after larger earthquakes. Shallow SSEs occur only after a sequence of partial rupture events, presumably to relax the stress induced by the preceding sequence. The peak slip rate of the shallow SSEs is an order of magnitude lower than that of the deep SSEs (Figs. S4a-b). Both shallow and deep SSEs are often followed by a sequence of partial rupture events, similar to the observation of aseismic slip preceding small to moderate earthquakes (e.g., Linde et al., 1988; Thurber, 1996; Thurber & Sessions, 1998).

We note, however, that the modeled earthquake sequences eventually become cycle-invariant after ~ 1750 years of simulation time (Fig. S5), even in the aging law reference model. This transition from aperiodic to periodic cycles implies that the complexity introduced by heterogeneous initial conditions can persist over multiple cycles, but is eventually erased even in the most complex considered models. Sustained complexity can be produced by explicitly accounting for fault roughness (e.g., Cattania & Segall, 2021; Tal & Gabrieli, 2024). Nevertheless, we find that the triggering responses do not notably depend on cycle complexity. We compare triggering response estimates from target mainshocks before and after the 1750 years transition and do not find any clear distinction between the two groups.

Due to the periodicity, we observe repeating earthquakes (i.e., repeaters; Uchida & Bürgmann, 2019) after the 1750 years transition, e.g., the two unlabeled events preceding event 246 and event 265 in Figure 6a. These repeaters occur at a depth of 11.36 km with a recurrence interval of 152 years. The repeaters in our model show a significantly smaller slip (~ 0.3 m) than that expected from the creeping velocity at the VS area surrounding the repeater asperity (~ 5 m), similar to observations of natural repeaters (e.g., Chen et al., 2007; Nadeau & Johnson, 1998). Thus, our model results raise caution using repeaters to infer local creep rates (Turner et al., 2024).

We assess the effect of using different evolution laws on the triggering estimates. The model assuming slip law is shown in Figure 6b. This model uses the same set of parameters as used in the aging law reference simulation, but with an increased $\overline{D_{RS}}$ of 10 mm to reduce the computational burden (see Supplementary Section S1). The modeled earthquake sequence is characterized by the repetition of a partial rupture event at the bottom of the seismogenic zone followed by a system-size earthquake in the middle of the seismogenic zone ($\sim$7 km). This model is denoted as the 'slip law reference model' hereafter. Since the input parameter of the slip law reference model is not identical to the aging law reference model, we perform an equivalent model with aging law using $\overline{D_{RS}} =$ 10 mm (denoted as 'A10 model' hereafter; Fig. 6c), for direct comparisons among different evolution laws. The A10 model and the aging law reference model differ in the magnitude of $\overline{D_{RS}}$ (10 mm vs. 2 mm).

The A10 model shows more complex earthquake sequences with multiple partial rupture events preceding system-size earthquakes compared to the slip law reference model. In the A10 model, a sequence of partial rupture events connected by a prolonged aseismic slip within the sequence leads to a system-size earthquake. Due to this prolonged aseismic slip, each foreshock-mainshock sequence in the A10 model lasts for 5.4 months on average, which is much longer than the 9.6 seconds in the slip law reference model or 11.7 hours in the aging law reference model.

Previous numerical studies comparing the slip patterns from the aging law and the slip law also noticed highly periodic earthquake sequences with a lack of smaller earthquakes when using the slip law (e.g., Rice & Ben-Zion, 1996; Rubin, 2008). This lack of complexity in slip law simulations is likely related to its slower growth of fracture energy during rupture acceleration, allowing instability under a smaller length scale as reflected in its smaller critical nucleation size (Ampuero & Rubin, 2008; Rubin, 2008). Additionally, once rupture initiates, the more aggressive dynamic weakening in the slip law may make it easier for the rupture to propagate across the entire fault (Ampuero & Rubin, 2008) whereas the aging law is more prone to rupture arrest when encountering VS patches, which act as barriers.

3.3 Triggering Responses: Aging Law

We perturb the aging law reference model (i.e., $\overline{D_{RS}} = 2$ mm) following the procedure outlined in Section 2.3. We consistently obtain several hours of target mainshock clock advance ($\Delta t > 0$) for all considered cases (Fig. 7). For example, we select various target mainshocks with hypocenter depths ranging from 4.34 km to 7.82 km while fixing the stress perturbation from the dynamic rupture model with the vertical foreshock fault, slow initiation with the mainshock fault strike of 340° (denoted "VSI, 340° strike" model), to explore the effect of target mainshock selection on the estimated triggering response. The observed clock advance ranges from 4.5 hours to 6.1 hours.

Next, we apply various stress models to a fixed target mainshock (event 282, 7.82 km depth; Fig. 6a) and observe time advances of several hours (4.1 hours to 5.6 hours) for all considered combinations of fault geometry and rupture characteristics. We repeat the process with different fixed target mainshocks (event 120, 6.5 km depth; event 88, 4.38 km depth), and the overall pattern of several hours of clock advance remains consistent.

Given the consistent behavior observed across all combinations of the perturbation model and target mainshock depths, we next explore the effect of the timing of the perturbation (i.e., t_g). We test seven different values for t_g (10 years, 1 years, 30 hours, 20 hours, 16.2 hours, 5 hours, and 1 hour) and perturb a fixed combination of the target mainshock (event 88, 4.38 km depth) and stress perturbation model (VSI, 340° strike; Fig. 8). The mainshock clock is advanced for all explored timings of perturbation. Our models show Δt decreases as t_g decreases (Fig. 8b). However, we do not observe instantaneous triggering even when the perturbation is applied closer to the unperturbed target mainshock time (e.g., $t_g = 1$ hours).

We further examine the control of t_g on the mainshock clock change by defining the 'closeness to instantaneous triggering' as $\Delta t/t_g$, a quantity designed to become 1 when the mainshock is triggered instantaneously (squares in Fig. S6). The closeness to instantaneous triggering varies non-linearly for different t_g and does not exhibit a clear trend with varying t_g values. This contrasts with previous simulation results with static ΔCFS perturbations showing a systematic convergence toward the instantaneous triggering curve as t_g decreases (Gallovič, 2008; Perfettini et al., 2003a). Our results imply that applying the stress perturbation later in the unperturbed earthquake cycle does not guarantee more rapid nucleation, likely due to the complexity of our models.

Earthquake triggering may also depend on the amplitude of the stress perturbation (Gallovič, 2008; Perfettini et al., 2003b; Wei et al., 2018). To explore the effect of the amplitude of the perturbing stress changes, we scale the amplitude of our stress perturbation by a factor ranging from 1 to 30 and perturb a given target mainshock (event 88). The amplification results in a wide range of the peak dynamic ΔCFS at the given target mainshock hypocenter location (4.38 km), from 0.5 MPa to 17.5 MPa. For smaller amplification factors (1, 2, 3, and 5), the mainshock clock is advanced but we do not observe instantaneous triggering. The magnitude of clock advance is systematically increased from 6.1 hours to 11.9 hours as the amplitude of the perturbing stress change is elevated.

The target mainshock is not triggered instantaneously, even when the stress perturbation is amplified by a factor of 10, yielding a peak dynamic ΔCFS of 5.8 MPa at the expected hypocenter depth. This peak dynamic ΔCFS value is equivalent to 27% of the excess strength during the quasi-static nucleation ($\tau - f_0\sigma_n = 21.4$ MPa for $\sigma_n = 53$ MPa at the nucleation site). Instead, a new partial rupture event that would not have occurred with the absence of perturbation is triggered soon after the perturbation (new event 1 in Fig. 9a), followed by a smaller partial rupture event (new event 2 in Fig. 9a), forming a new sequence that does not culminate in a system-size earthquake. A system-size earthquake occurs several months after the sequence at a slightly shallower depth, eventually delaying the time by 74 days compared to the unperturbed model. However, since the sequence that leads to the mainshock is completely altered, we do not consider the new system-sized event as a delay of the target mainshock but rather consider it as a new event not observed in the reference model.

The instantaneous triggering of a system-size earthquake occurs when the stress perturbation is amplified by a factor of 30, resulting in a peak dynamic ΔCFS of 17.5 MPa at the mainshock hypocenter depth (Fig. 9b). This peak dynamic ΔCFS value corresponds to 82% of the excess strength during the quasi-static nucleation. We consider this event as an example of dynamic triggering since it nucleates ~ 2.5 seconds after the start of perturbation, which corresponds with the arrival of the largest dynamic stress. The depth of the nucleation also matches that of the peak dynamic stress change.

Throughout the exploration with our aging law reference model, we persistently obtain a mainshock clock advance. To understand the underlying physical mechanisms, we examine the correlation of the clock advance with five key physical parameters (Fig. 7): peak dynamic ΔCFS and static ΔCFS at the depth of maximum slip during the perturbation period (i.e., at $z_{max} = \text{argmax}_z\, \delta(z)$ for slip δ), peak slip, peak slip rate, and work per distance (W; Eq. (13)) along the entire fault.

We define work per distance W as the work density integrated over the entire fault:

$$W = \int_0^{L_f} \int_0^{\Delta\delta(z)} \Delta\tau(z,\delta)\, d\delta dz, \tag{13}$$

where δ is slip, $\Delta\delta$ and $\Delta\tau$ are the net slip and shear stress change during the perturbation period, respectively. Although W includes all VW and VS regions, the contribution of creep in VS regions ($V \sim 10^{-9}$ m/s) is minor compared to that in VW regions ($V \sim 10^{-6}$ m/s) to W. The W metric well captures the net energy gain or loss due to the applied stress perturbation along the fault. This metric measures a combined effect of external stress change and inherent slip together along the entire fault. We compute the Pearson correlation coefficient R between the Δt and each parameter for a quantitative comparison.

The clock advances from our models show a strong correlation with both peak dynamic ΔCFS and static ΔCFS values, showing R values of 0.86 and 0.94, respectively. Both parameters show a positive, almost linear, relationship with the clock advance. In contrast, the peak slip, the peak slip rate, and the work per distance did not show a strong correlation with the estimated clock advance ($R \leq 0.53$). However, it is worth noting that all W values are positive for all clock advance models. As will be discussed in more detail in Section 4.3, the sign of the W value effectively predicts whether the mainshock will advance or delay as a response to the given stress perturbation.

Note that we measure both ΔCFS values at z_{max} instead of the hypocenter depth in the unperturbed models. This choice is made to fully reflect the ongoing aseismic slip at the time of perturbation in our models, mostly in the form of afterslip of the preceding foreshocks (see Figs. 12a & 12b). Thus, the depth of maximum slip during the perturbation period indicates the depth of the most rigorous aseismic transient deformation. We will discuss more about this choice in Section 4.3.

3.4 Triggering Responses: Other Evolution Laws

In the previous section, our models with aging law consistently predict the clock advance of the next large event regardless of the choice of event, stress perturbation model, and timing of perturbation, unless the amplitude of perturbing stress is significantly elevated to produce instantaneous triggering. In this section, we explore triggering responses from other state evolution laws.

Although adding the stress-dependent term in the evolution law (i.e., the last term in Eq. (11)) is expected to make the models more realistic, it is still poorly understood how this stress-dependency affects the state variable evolution on a fault with a complex seismic and aseismic slip history and in turn, how it would affect the triggering response on the fault. Thus, we estimate the triggering response with stress-dependent aging law, following the procedure outlined in Section 2.3, and compare the results with those from the aging law reference model. The stress-dependent aging law and aging law reference model take the same unperturbed model (i.e., aging law reference model), but differ in that the stress-dependent term is applied during the perturbation period for the stress-dependent aging law models. We again obtain mainshock clock advances of several hours (i.e., $\Delta t > 0$) when using the stress-dependent aging law, but the former are systematically smaller compared to the aging law reference model (Fig. 10). For example, a given combination of target mainshock (event 282, 7.82 km depth) and the stress perturbation model (VSI, 340° strike) yields $\Delta t = 4.5$ hours when perturbing the aging law reference model while $\Delta t = 3.7$ hours is obtained using the stress-dependent aging law (Fig. 10a). The decreased magnitude of clock advance in stress-dependent aging law is robustly obtained for all five tested cases with different target events and stress perturbation models (Fig. 10b).

The reduction of clock advance can be well explained in the framework of work per distance (W). With the stress-dependent term, the evolution of the state variable and the slip rate during the perturbation period resembles that of the external stress perturbation, leaving a depth-dependent static change in both variables. Therefore, tracking the change in variable at a single depth cannot fully explain the systematic decrease in Δt. We rather compute the W values from the stress-dependent law models, which reflect integrated effect along the entire fault, and obtain systematically lower W values compared to the aging law reference models (Fig. 10c). Since models using different evolution laws are perturbing the same target mainshock using the same stress perturbation, the reduction in W originates from the amount of slip at regions under higher ΔCFS values. Integration of the state variable in Eq. (11) leads to a minor decrease in slip in our stress-dependent law models, thus causing slightly smaller advances of the time of mainshock. This result emphasizes again the importance of considering the fault as a whole.

Next, we explore whether using the slip law (Eq. (10)) significantly alters the triggering response, since the slip law may facilitate triggering compared to the aging law owing to its smaller nucleation size. We perturb our slip law reference model with different stress perturbation models and obtain a similar pattern of clock advance of several hours, ranging from 6 to 8 hours. We cannot explore the effect of hypocenter depth since the slip law reference model produces a repetitive sequence with a single hypocenter depth (6.92 km) for system-size events. The clock advance of 6 to 8 hours is comparable to that of 5 to 9 hours estimated from the aging law reference model using a system-size event with a similar depth of 6.5 km. However, we cannot directly compare the Δt value between the slip law reference model and the aging law reference model due to their different parameter setups.

For a better comparison, we perturb the A10 model with different stress perturbation models, and surprisingly, we consistently obtain mainshock clock delays (i.e., $\Delta t < 0$) instead of advances. To understand the key control of clock advance versus delay, we investigate the five key parameters examined in Figure 7 for both clock advance and clock delay models (Fig. S7). We observe that the static ΔCFS value and W value exhibit a clear distinction between the clock advance models and the clock delay models. All clock delay models from the A10 model show negative values for both parameters, in contrast to all clock advance models, which show positive values. The notable contrast in the static ΔCFS value and W value implies a strong control of the combined effect of the static ΔCFS and background aseismic slip along the entire fault on the mainshock clock change. We discuss this combined effect in detail in Section 4.3.

The only deviation between the sign of W and the sign of Δt occurs when the perturbation is applied long before the target mainshock (i.e., larger t_g). We obtain a mainshock clock delay of ~ 13 years when we increase t_g to 30 years, unlike the clock advances obtained from smaller t_g values (Fig. S13). Then, the estimated W value is very small but positive, an unexpected outcome for a model with a mainshock clock delay. Using $t_g = 30$ years, the perturbation is applied before the first transient in a sequence of SSEs occurring in the deeper part of the seismogenic zone, preceding the target foreshock-mainshock sequence. This perturbation triggers a new SSE, which ultimately delays the target mainshock's onset. This implies that the external energy applied at $t_g = 30$ years is insufficient to affect the nucleation of the foreshock-mainshock sequence but instead is consumed in initiating an additional aseismic transient. The unpredictable behavior associated with the complex SSE sequence emphasizes the importance of considering aseismic processes in the context of longer seismic cycle history.

In addition, we find a decrease of Δt value when using the stress-dependent aging law to perturb the A10 models. For example, we obtain 6 hours of time delay (i.e., $\Delta t = -6$ hours) when perturbing target mainshock 18 in the A10 model using the VSI stress perturbation model with the mainshock strike orientation of 340°. When assuming the stress-dependent aging law during the perturbation period, the time delay increases to 6.5 hours (i.e., $\Delta t = -6.5$ hours). This result suggests that the stress-dependent term systematically decreases Δt value, regardless of its sign.

4 Discussion

4.1 Lack of Instantaneous Triggering

Throughout this study, we persistently observe a lack of instantaneous triggering. In Section 3.3, we find that instantaneous triggering is not obtained even for small values of t_g and that the proximity to instantaneous triggering is unpredictable. Some studies suggest that a larger perturbing stress amplitude leads to a more rapid convergence toward instantaneous triggering as t_g decreases (Gallovič, 2008; Gomberg et al., 1998; Perfettini et al., 2003a, 2003b). To analyze such amplitude dependency, we repeat the analysis detailed in Section 3.3 with a stress perturbation amplitude elevated by a factor of 5 (resulting in a peak stress change of ∼3 MPa at the expected target hypocenter depth; triangles in Fig. S6). As expected, the overall proximity to instantaneous triggering increases with elevated amplitudes. However, the proximity to instantaneous triggering systematically decreases with smaller t_g values, indicating less efficient triggering when the perturbation occurs later in the cycle. The non-monotonic response of Δt for varying t_g may be explained as a combined contribution from transient (larger Δt value when applied later in the cycle) and static (smaller Δt value when applied later in the cycle) stress changes, as suggested by Gomberg et al. (1998). Both simulation cases demonstrate that the timing of the perturbation is not a crucial factor in instantaneous triggering.

In our model parameterization, instantaneous triggering occurs only when the peak amplitude of stress perturbation at the unperturbed mainshock hypocenter depth is elevated to 17.5 MPa (30-times elevated model; Fig. 9b). We identify instantaneous triggering as dynamically triggered based on the occurrence time and hypocentral depth, which coincide with the arrival of the peak dynamic ΔCFS . The amplitude required for instantaneously triggered rupture in this study (17.5 MPa) is consistent with the additional prestress level required to dynamically nucleate the Ridgecrest mainshock after the M_w 6.4 foreshock (18 MPa), estimated from a realistic sequence of 3D dynamic rupture simulations (Taufiqurrahman et al., 2023). The required peak stress change amplitude of a few tens of MPa is also consistent with the dynamic triggering threshold inferred from peak seismic velocities (Gomberg et al., 2001). This amplitude (17.5 MPa) is slightly less than, but comparable to, the steady-state-to-peak stress change of 20.4 MPa produced by the unperturbed model. This implies that the amplitude of the stress perturbation is comparable to the excess strength during the quasi-static nucleation for an instantaneous dynamic triggering to occur (Fig. S14). Because the excess strength scales with the effective normal stress, this may explain why dynamically triggered earthquakes are mostly observed in geothermal areas (Aiken & Peng, 2014; Brodsky & Prejean, 2005; Hirose et al., 2011; Husen et al., 2004), where the effective normal stress may be locally low due to the presence of over-pressurized fluids. The triggering stress required in our perturbed model is somewhat lower ($< 90\%$) compared to the strength excess, indicating that the passage of seismic waves may additionally affect the effective fault strength.

Most of the delayed triggering cases we model are strongly influenced by the static stress change (Section 4.2). The dominance of the static stress change in earthquake triggering was suggested in previous studies as well. High-precision earthquake catalogs reveal a lower triggering threshold for static stress change than the dynamic stress change (Gomberg et al., 2001) or a strong size-to-distance relationship of aftershocks (van der Elst & Shaw, 2015). Also, a delayed change in seismicity rate, particularly a delayed decrease in seismicity rate, can be well explained by the static stress transfer (Kroll et al., 2017; Toda et al., 2012). In numerical simulations with rate-and-state friction law, a higher triggering potential of the static ΔCFS compared to the dynamic ΔCFS of the same amplitude is reported for fast and slow earthquakes (Belardinelli et al., 2003; Gomberg et al., 1998; Luo & Liu, 2019; Yoshida et al., 2020).

We find that a peak dynamic ΔCFS of moderately large amplitude (~ 5.8 MPa at the unperturbed hypocenter depth) is capable of triggering partial ruptures which alter the stress distribution along the fault, subsequently leading to an entirely new sequence of earthquakes following the perturbation (Section 3.3; Fig. 9a). From a seismic hazard perspective, our models may imply that an earthquake is less likely to be triggered immediately by another earthquake unless an exceptionally high amplitude of stress is transferred. However, a significantly strong perturbation may affect the occurrence of smaller earthquakes, causing changes in the timing and location of nucleation of the next large earthquake in a highly non-linear, complex way.

4.2 Which is Dominant in Earthquake Triggering: Static or Dynamic Stress Changes?

Identifying the roles of static and dynamic stress changes in earthquake triggering is important for seismic hazard assessment, specifically in the aftermath of large earthquakes. We aim to understand the relative contribution of each process. Our models contain both dynamic and static components of ΔCFS and provide insights into their combined impact on the mainshock clock change.

We now compare how the Δt estimates from our models change when we perturb using only the dynamic component of the ΔCFS or only the static component. First, we separate the dynamic and static components of the ΔCFS from the "VSI, 340° strike" stress perturbation model by tapering out the early ($t < 10$ seconds) or late ($t < 10$ seconds) part of the computed time series of dynamic stress perturbations due to the M_w 5.4 foreshock (Fig. S8).

In Figure 11, we compare the triggering response from dynamic-only and static-only models with that from the original stress perturbation model, which includes both dynamic and static components. When both components are included, we obtain a mainshock clock advance of 4.5 hours. In contrast, the mainshock clock advances only by a few seconds (3.9 seconds) when we perturb with the dynamic-only perturbation model. The static-only perturbation model almost fully reproduces the mainshock clock advance of 4.5 hours. The Δt estimates of the original model and static-only model differ by only 1.4 seconds. The dominance of static ΔCFS is robust when tested with different sets of target mainshocks and stress perturbation models. Thus, we conclude that static ΔCFS is more effective in altering the timing of a future mainshock in our model setup.

However, the limited contribution from the dynamic ΔCFS in our models cannot fully explain the frequent observation of dynamic triggering, particularly in the far field. The lack of dynamic triggering in our models might be related to the short duration ($<$ 5 seconds) of the dynamic ΔCFS used in this study (Katakami et al., 2020; Wei et al., 2018). Additional weakening mechanisms that are not considered in our models, such as pore pressure changes, thermal pressurization, localization of brittle deformation, or off-fault damage, may play a crucial role in facilitating dynamic triggering (e.g., Brodsky et al., 2003; Elkhoury et al., 2006; Gabriel et al., 2024; Zhu et al., 2020).

Another mechanism that may contribute to the complexity of earthquake triggering is the cumulative stress transfer from multiple foreshocks. We observe a systematic shortening of the duration of the cascading foreshock-mainshock sequence in our models as a result of perturbation. For example, the duration of the foreshock-mainshock sequence (i.e., time from the leading foreshock to the system-size earthquake) in one of the sequences in the unperturbed aging law reference model is 1166 seconds, which becomes 411 seconds when it is perturbed (Fig. S9). Similar behavior has been shown in models with a rough fault surface, where creep was accelerated in areas of low effective normal stress due to foreshocks (Cattania & Segall, 2021). This shortening of the sequence implies that the superposition of perturbations from multiple foreshocks might significantly advance the mainshock occurrence time. While this study only considers the stress changes inferred from the closest M_w 5.4 foreshock, the 2019 Ridgecrest mainshock was accompanied by multiple foreshocks, including the largest M_w 6.4 foreshock (e.g., Meng & Fan, 2021; Ross et al., 2019; Shelly, 2020). Although a single foreshock's perturbation may not be sufficient to dynamically trigger the mainshock, it might be possible to dynamically trigger the mainshock if the fault is sufficiently weakened due to prior seismicity.

4.3 What Controls the Mainshock Clock Change?

We investigate the dominant factors controlling the sign of the Δt estimate in our models. First, to confirm that the mainshock clock change in the complex sequences of seismic and aseismic events cannot be fully explained by a simple analytic solution, we compare the change in time to instability (defined as $t_i = t_g - \Delta t$) measured from our simulations to that predicted from a 1D spring-slider solution (Fig. S10; Dieterich, 1994). Although we do not follow the exact formula, we adopt the concept that an increase in stress may lead to an increase in slip rate and a reduction of the time to instability, acknowledging that our complex model setup and the 1D spring slider solution are not directly comparable.

In our analysis, we apply the perturbation at $t_i = 16.2$ hours before the target mainshock (event 282). After the perturbation, we measure a t_i of 11.7 hours in one of our models using the "VSI, 340° strike" stress perturbation. The perturbation causes a quasi-constant increase in the slip rate of 4.8×10^{-8} m/s. Tracking the time in the unperturbed model when this increased slip rate is reached yields a much shorter time to instability (t_{D94}) of 2.7 hours. The deviation of time to instability from the analytical solution has been documented for complex models, particularly for those involving a rheological transition from VW to VS (Kaneko & Lapusta, 2008), agreeing well with our models with multiple VW-to-VS transitions along the fault. The large discrepancy between these two estimates indicates that simple analytic solutions may not be suitable for predicting the triggering response on natural faults with complex earthquake- and slow-slip transient history.

To discuss the question of what may control the mainshock clock change on a complex fault, we compare models that show clock advance and clock delay. The clock advance and delay are obtained by perturbing target mainshocks at similar hypocentral depths (4.38 km and 3.7 km) in either the aging law reference model or the A10 model, respectively, using the same stress perturbation (VSI, 340° strike). The perturbed aging law reference model yields a clock advance of 6 hours (Fig. 12a), while the perturbed A10 model yields a mainshock clock delay of 6 hours (Fig. 12b).

The key difference between these two cases lies in the depth extent of the ongoing aseismic slip at the time of the perturbation. The clock delay model shows a wider zone of aseismic slip ranging from ∼7 to 15 km, while the clock advance model shows a narrower zone of aseismic slip confined near ∼11 km depth. This difference arises from the month-long foreshock sequence in the A10 model, although the two models share the same t_g of 16.2 hours.

We recall that the static stress shadow occurs between 5 km and 10 km depth, overlapping with the depth extent of the aseismic slip in the clock delay model but not in the clock advance model (Fig. 12c). Since the perturbation does not induce significant slip, the ongoing aseismic slip controls the net amount of work done by each fault (i.e., δ in Eq. (13)). If the fault slips within the static stress shadow, it loses energy (i.e., negative W), delaying the next earthquake (Fig. S7e). Conversely, in the clock advance model, the fault gains energy, promoting the onset of the next earthquake.

To probe the robustness of this behavior, we perturb the same event in the aging law reference model with a much smaller t_g of 2 minutes, the time at which the afterslip from foreshocks is extended to the static stress shadow. Despite the proximity to the unperturbed event time, we observe a clock delay of 82 seconds, accompanied by a negative W value. This suggests that the complex interplay between background deformation and external stress perturbation governs the advancement and delay of a future large event.

We conduct two additional sets of simulations to verify that our findings are not dependent on our specific choice of parameters. In one of the two model setups, a slower loading velocity of 3.2×10^{-11} m/s is used (Fig. S11a), and in the other model, a different fractal distribution with $\lambda_{min} = 30$ m (order of L_∞) and $\lambda_{max} = 10$ km (order of seismogenic zone width) is used for all three parameters (σ_n^0,$(a-b)$, and D_{RS}; Fig. S11b). Both models involve foreshock-mainshock sequences connected by afterslip but with a different recurrence interval (from ~ 76 years in higher V_{pl} to ~ 1915 years in lower V_{pl}) and spatial pattern of afterslip. For a diverse combination of target mainshocks in both models and different stress perturbations, we obtain several hours of time advance when W is positive while we obtain several days of time delay when W is negative. Thus, we conclude that the control of the sign of the static ΔCFS under regions of active aseismic slip on the mainshock clock advance and delay is not restricted to the specific set of parameters used in Section 3.

We find that the change in the mainshock clock is mostly controlled by the aseismic transfer of energy instead of the direct change from the perturbation itself. We explore how the fault friction evolution changes due to the perturbation by plotting a phase diagram (Fig. 13; Belardinelli et al., 2003; Dublanchet et al., 2013; Noda et al., 2009; Rice & Tse, 1986). We find that the fault is neither significantly brought closer to nor farther from the steady state during the perturbation period (pink lines in Fig. 13). Instead, the perturbed evolution curve deviates from the unperturbed evolution curve before the start of the foreshock-mainshock sequence (i.e., shallow SSE period; Fig. 13a) and during the foreshocks (Figs. 13b-c). During the mainshock, however, the evolution of friction in the perturbed and unperturbed models appears comparable (Fig. 13d).

We observe similar behavior across several different scenarios, including the same target mainshock and stress perturbation pair with stress-dependent friction law and the clock delay model. The phase diagram suggests that foreshocks and aseismic slip can accommodate the changes induced by external perturbations, allowing the mainshock to follow a nearly identical limiting cycle.

Our results highlight the crucial role of the interaction between external stress perturbations and ongoing background slip in earthquake triggering (Gallovič, 2008; Inbal et al., 2023; Kostka & Gallovič, 2016) in complex earthquake sequences with realistic stress perturbations, suggesting caution when assessing the triggering potential of future earthquakes. For example, focusing solely on the unperturbed mainshock hypocenter area could be misleading. The static ΔCFS in our models often show negative values, even in cases where the mainshock clock advances, if measured at the target mainshock hypocenter depth in the unperturbed models (Fig. S12; compare this with Fig. 7b), which may seem counter-intuitive. However, the mainshock can be still be promoted by complex stress-slip interaction on other parts of the fault, even when the external stress perturbation locally discourages triggering at the hypocenter. We propose that, instead of focusing on a specific location, it is more appropriate to consider the entire fault (e.g., by analyzing W) when estimating a triggering response, although such an approach would require some prior knowledge on the spatial heterogeneity of the rate-and-state frictional parameters.

5 Conclusions

We combine dynamic rupture simulations and seismic cycle simulations to estimate the triggering response of the 2019 M_w 7.1 Ridgecrest mainshock to the stress perturbation from the M_w 5.4 foreshock. Detailed spatiotemporal stress changes near the mainshock nucleation site are computed using 3D dynamic rupture simulations, accounting for various fault geometries (mainshock fault strike and foreshock fault dip) and foreshock rupture dynamics.

Our 2D quasi-dynamic seismic cycle simulations show that a broad spectrum of fault slip including both system-size and partial ruptures on the mainshock fault occurs only when multiple fractal heterogeneities in both stress and strength parameters are introduced conjointly. In addition to a high W_S/L_∞ ratio, VS patches are key to depth-variable earthquake nucleation along the entire seismogenic zone, causing elevated stressing rates at their margins. Our reference model features system-size earthquakes with a range of hypocentral depths that are always preceded by a cascade of partial ruptures, as well as shallow and deep SSEs. However, the reference sequence transitions from aperiodic to periodic cycles after thousands of years, implying that the complexity introduced by heterogeneous initial conditions is gradually erased over multiple cycles.

Perturbing the seismic cycle models using the dynamic and static stress changes from the dynamic rupture simulations consistently results in a mainshock clock advance of several hours in most cases. Aging and slip law models show comparable mainshock clock advances, while stress-dependent aging law models exhibit a systematic reduction in clock advance.

Instantaneous triggering occurs only when the peak ΔCFS at the unperturbed hypocenter depth is increased to 17.5 MPa, comparable to the excess stress during the quasi-static nucleation. The timing of the perturbation has little impact on instantaneous triggering or the mainshock clock change. In some cases, triggering is less efficient when the perturbation is applied later in the cycle.

Our findings indicate a dominant influence of static ΔCFS on the mainshock clock change. Models perturbed using only the static component of stress change closely reproduce the mainshock clock change seen in models with both dynamic and static components, whereas the dynamic ΔCFS component alone results in a minor clock advance of only a few seconds.

Finally, we explain the mainshock clock advance and delay across all explored cases by the sign of the static ΔCFS in areas of accelerating slip, quantified by the W metric. Additionally, we find that a mainshock can be promoted if the entire fault gains energy under the stress perturbation (i.e., positive W), even when the future mainshock hypocenter depth is in a local static stress shadow. This effect may be driven by stress transfer from foreshock sequences and/or aseismic slip. Our results highlight the critical role of foreshock sequences and aseismic deformation in earthquake triggering and emphasize the importance of considering the physics of fault-system-wide, short- and long-term processes when assessing triggering potential.

Table 1. Parameters for the 3D dynamic rupture simulation using *SeisSol*. VFI: vertical foreshock fault, fast initiation; VSI: vertical foreshock fault, slow initiation; DFI: dipping foreshock fault, fast initiation; DSI: dipping foreshock fault, slow initiation.

Symbol	Parameter	Value			
		VFI	VSI	DFI	DSI
D_{LSW}	Critical slip-weakening distance	0.1 m	0.25 m	0.1 m	0.25 m
f_d	Dynamic friction coefficient (nucleation patch)	0.3743	0.3343	0.3328	0.2735
	Dynamic friction coefficient (foreshock fault)	0.471	0.431	0.4295	0.3702
	Dynamic friction coefficient (mainshock fault)	1000			
f_s	Static friction coefficient (nucleation patch)	$0.4433 - 0.4869$			
	Static friction coefficient (foreshock fault)	$0.5841 - 0.7$			
	Static friction coefficient (mainshock fault)	1000			
$\boldsymbol{\sigma}_{xx}$,$\boldsymbol{\sigma}_{yy}$,$\boldsymbol{\sigma}_{zz}$	Normal components of the initial stress tensor	120 MPa			
$\boldsymbol{\sigma}_{xy}$	Along-strike shear component of the initial stress tensor	70 MPa			
$\boldsymbol{\sigma}_{yz}$,$\boldsymbol{\sigma}_{xz}$	Along-dip shear components of the initial stress tensor	0 MPa			
C_0	Frictional cohesion	0.2 MPa			

Table 2. Parameters for reference seismic cycle models using *Tandem*.

Symbol	Parameter	Value
a	Rate and state parameter, direct effect	Varies
b	Rate and state parameter, evolution effect	0.019
$\overline{D_{RS}}$	Average characteristic state evolution distance	2 mm or 10 mm
f_0	Reference coefficient of friction	0.6
V_0	Reference slip rate	10^{-6} m/s
V_{init}	Initial slip rate	10^{-9} m/s
V_{pl}	Plate loading rate	10^{-9} m/s
$\overline{\sigma_n^0}$	Average background effective normal stress	$10 - 50$ MPa
τ^0	Background shear stress	$10 - 30$ MPa
ν	Poisson's ratio	0.25
μ	Shear modulus of the elastic bulk	20 GPa
W_S	Seismogenic zone width	~ 10 km
L_f	Fault length	24 km

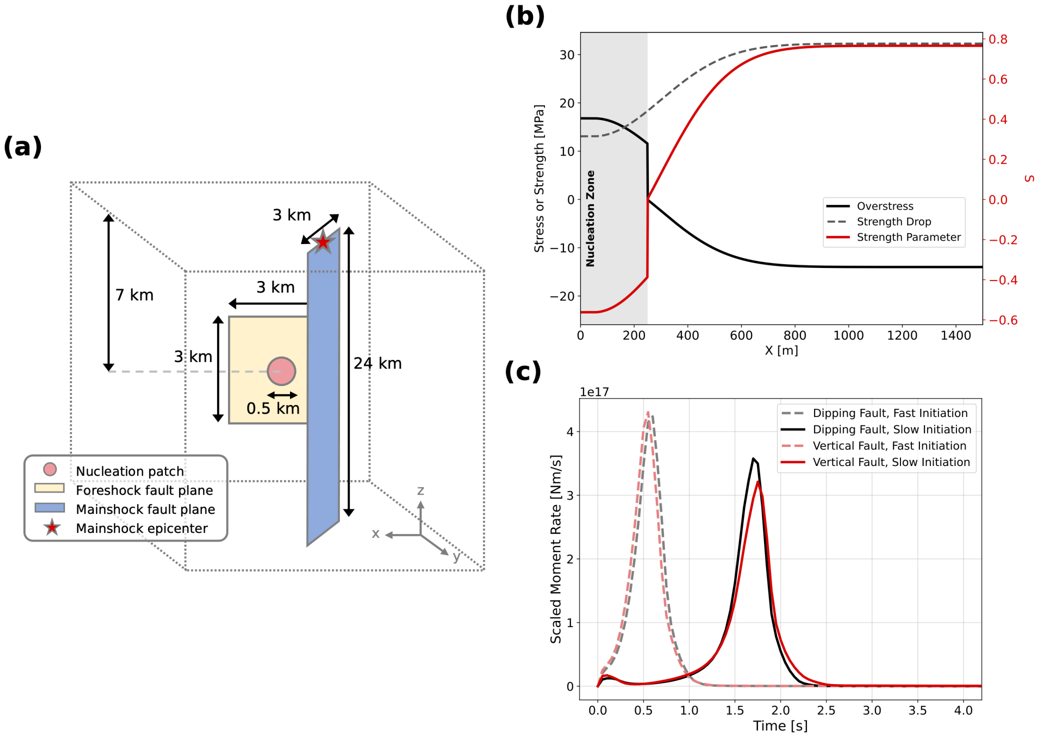

Figure 1. (a) Sketch of the model geometry for the 3D dynamic rupture simulation using *SeisSol*. The foreshock fault (yellow), mainshock fault (blue), and circular nucleation patch (pink) are shown. The red star denotes the location of the 2019 M_w 7.1 Ridgecrest mainshock epicenter. The sketch is not to scale with respect to depth (the z-axis). (b) An example of the prestress conditions used to nucleate the M_w 5.4 foreshock in the vertical foreshock fault and the slow initiation (VSI) model. The overstress (black line), the relative strength parameter S (red line), and the strength drop (grey dashed line) are shown along a profile across the foreshock plane from its center to its edge. The grey shaded area indicates the extent of the nucleation patch. (c) Moment rate functions for the four classes of dynamic rupture models, classified by the combination of rupture characteristics (dashed lines for fast initiation and solid lines for slow initiation) and the dip of the foreshock fault (red hues for vertical foreshock fault and black hues for dipping foreshock fault). The moment rates are scaled by the expected moment from an M_w 5.4 earthquake (i.e., $M_{5.4}$).

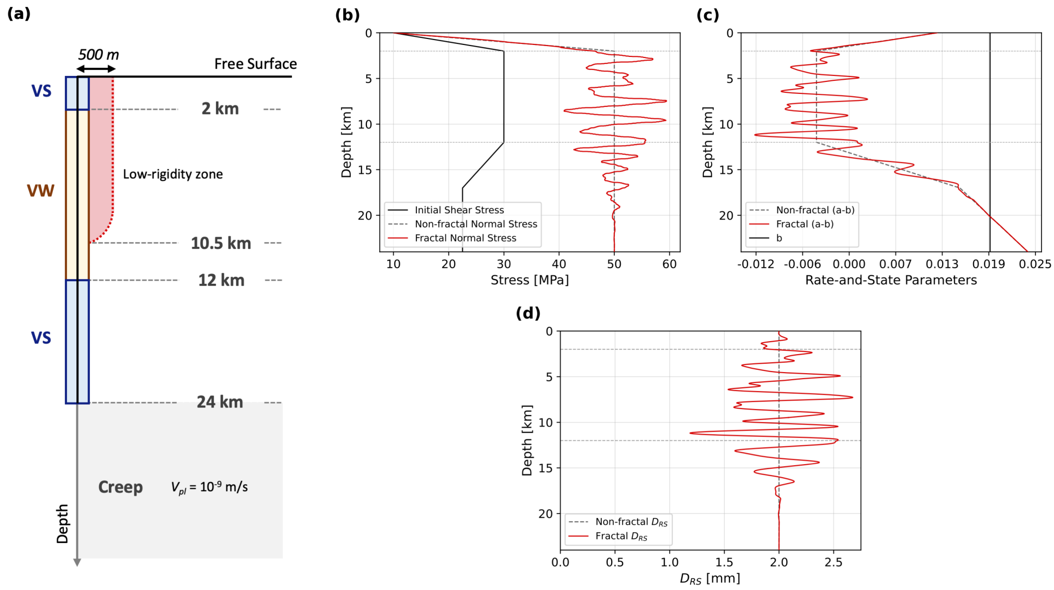

Figure 2. (a) Sketch of the model geometry for the seismic cycle simulations using *Tandem*. The rate-and-state fault (black vertical line) includes a central velocity-weakening zone (yellow) surrounded by shallow and deep velocity-strengthening zones (blue). The bottom creep zone governed by the constant loading rate (V_{pl}) is shaded in grey. The red-shaded area indicates the spatial extent of a low-rigidity fault zone included in additional models summarized in Supplementary Section S2. As the model represents a perfectly symmetric vertical strike-slip fault, we model only one side of the domain. (b-d) Self-affine fractal distributions of initial effective normal stress (b), rate-and-state parameters (c), and characteristic state evolution distance (d), that parameterize the aging law reference model. The fractal distributions of all three parameters share the same limiting wavelengths of $\lambda_{min} = 500$ m and $\lambda_{max} = 2.5$ km.

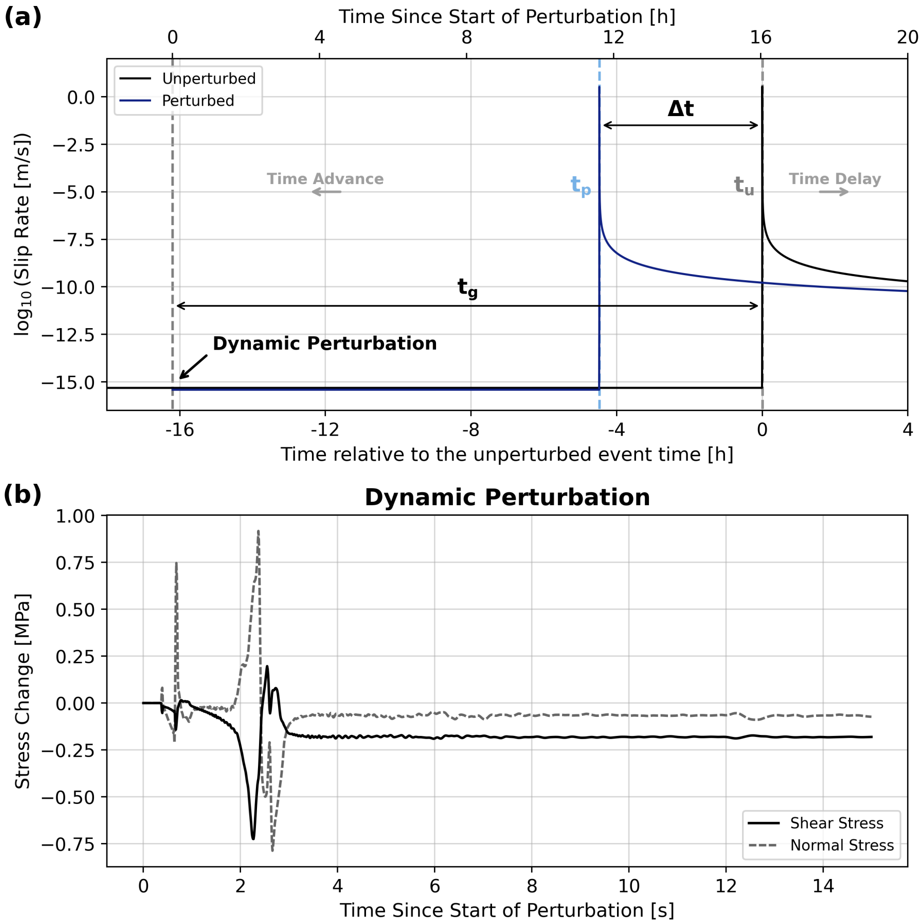

Figure 3. Illustration of the process for estimating the triggering response (Section 2.3). (a) Slip rate evolution of the unperturbed model (black) and the perturbed model (dark blue) at the mainshock hypocenter depth in the unperturbed model (7.82 km). Grey and light blue dashed lines indicate the time of the unperturbed (t_u) and perturbed (t_p) system-size earthquakes, respectively. The vertical arrow marks the timing of the applied dynamic perturbation, while the horizontal arrows represent the clock advance (Δt) and the time interval between the perturbation and the unperturbed mainshock time (t_g). (b) The applied dynamic stress changes at the depth of the unperturbed target mainshock hypocenter. The solid line represents the change in shear stress ($\hat{\tau}$), while the dashed line shows the change in normal stress ($\hat{\sigma_n}$). This example is generated by perturbing target mainshock event 282 (Fig. 6a) using the dynamic stress perturbation from the dynamic rupture model with the vertical foreshock fault, slow initiation (VSI) with 340° strike orientation of the mainshock fault.

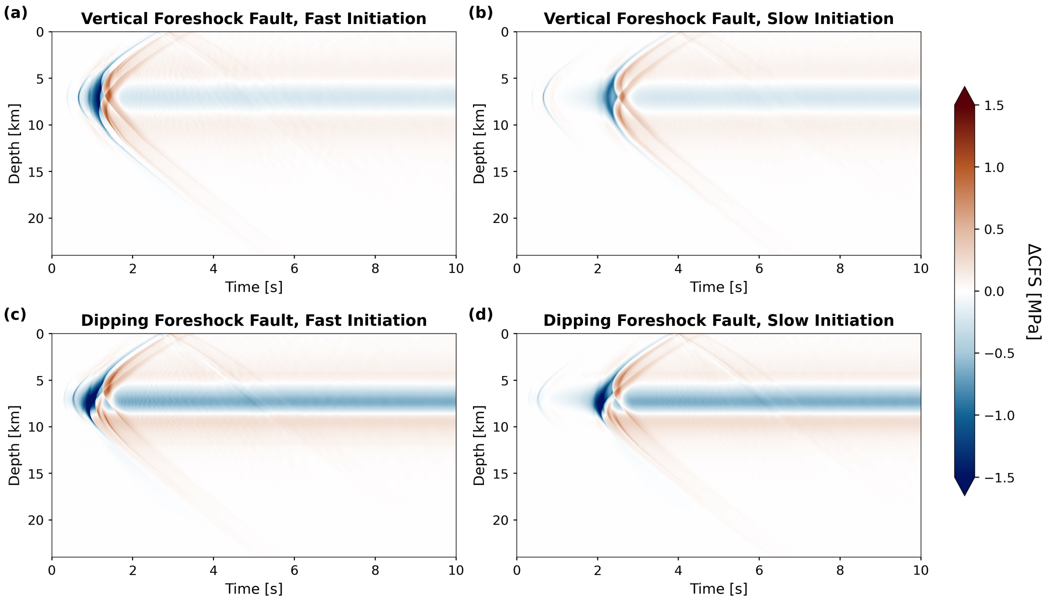

Figure 4. Spatiotemporal evolution of ΔCFS along the mainshock fault in 3D dynamic rupture models for (a) VFI, (b) VSI, (c) DFI, and (d) DSI models. All four models assume a mainshock fault strike of 340°. (VFI: vertical foreshock fault, fast initiation; VSI: vertical foreshock fault, slow initiation; DFI: dipping foreshock fault, fast initiation; DSI: dipping foreshock fault, slow initiation.)

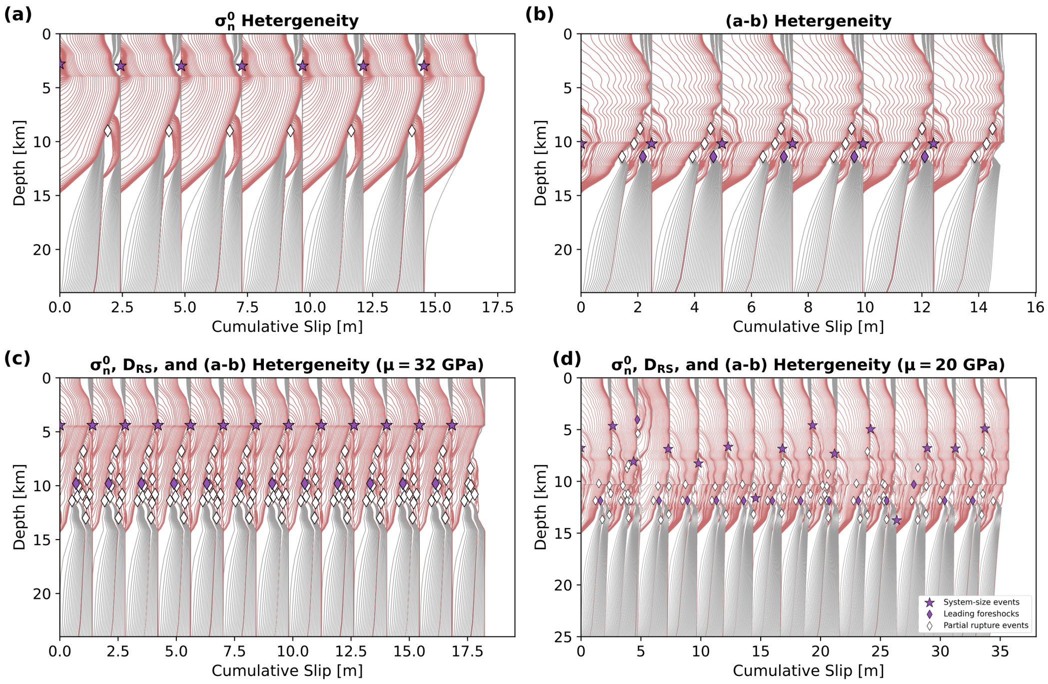

Figure 5. Cumulative slip evolution along the fault in exemplary seismic cycle simulations with initial stress and strength heterogeneity. (a) Seismic cycle model with heterogeneity only in initial effective normal stress (σ_n^0) using the fractal distribution shown in Figure 2b. (b) Seismic cycle model with heterogeneity only in the $(a - b)$ parameter, featuring velocity-strengthening patches embedded within the seismogenic layer using the fractal distribution shown in Figure 2c. (c-d) Models with heterogeneity in all three parameters using the fractal distributions shown in Figures 2b-d but with different shear moduli (μ) of 32 GPa (c) and 20 GPa (d). All models show the cumulative slip omitting the first 200 years of spin-up time. The model in (d) shows the first 1353 years of a 5000-year simulation. Pink contours, drawn every 0.5 seconds, show the coseismic evolution of slip, while grey contours, plotted every 2 years, show the longer-term evolution of slip. Purple stars, purple diamonds, and white diamonds indicate the hypocenter locations of system-size earthquakes, leading foreshocks, and partial rupture events, respectively.

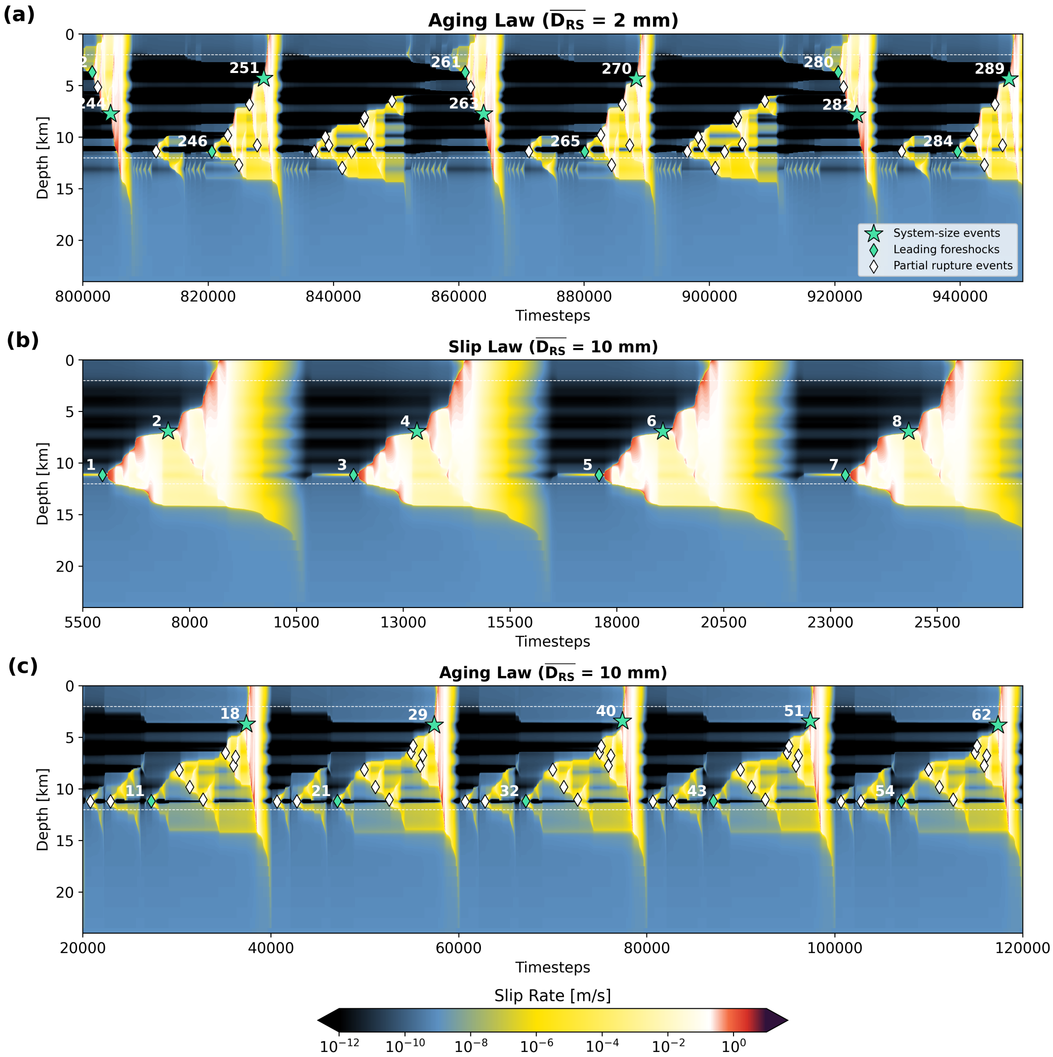

Figure 6. Spatiotemporal evolution of slip rate of reference seismic cycle models used in this study. (a) Reference aging law seismic cycle model, showing the period between 2317 years and 2681 years of simulation time. (b) Reference slip law seismic cycle model ($\overline{D_{RS}} = 10$ mm) and (c) the equivalent aging law model with $\overline{D_{RS}} = 10$ mm (A10 model; see Section 3.2). Event numbering starts from a non-zero value since we only show the spun-up phase of the models, i.e., after 200 years of simulation time. Green stars, green diamonds, and white diamonds indicate the hypocenter locations of system-size earthquakes, leading foreshocks, and partial rupture events, respectively.

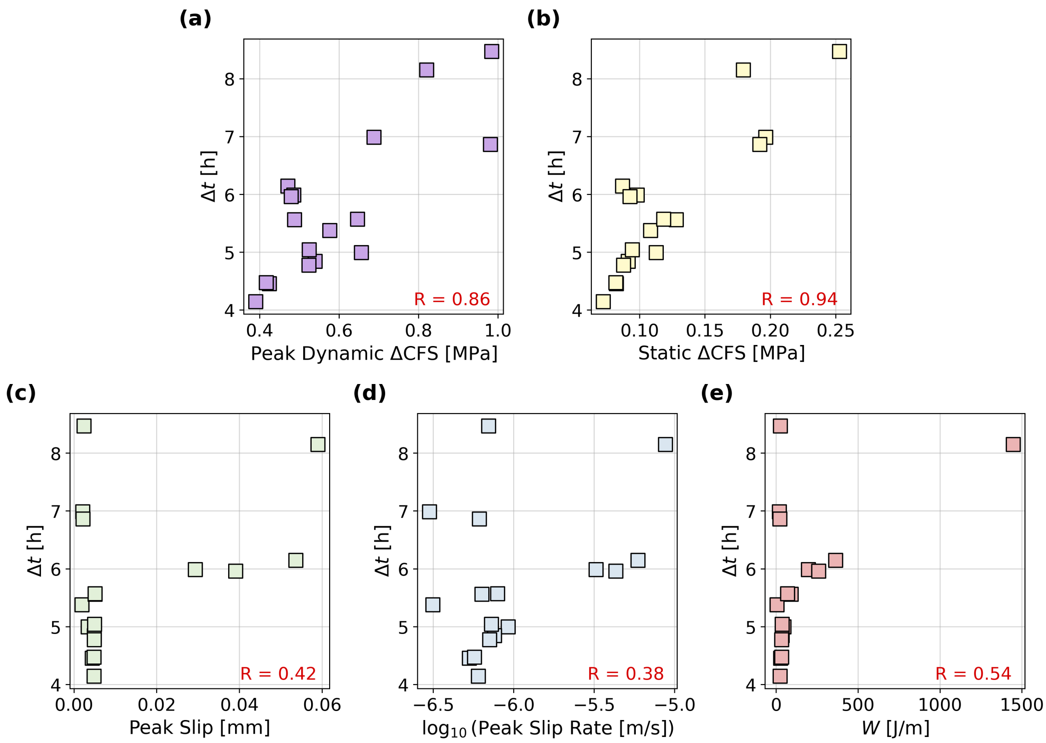

Figure 7. Correlation between the mainshock clock change (Δt) and various physical parameters obtained from all explored cases with the aging law reference model: (a) peak dynamic ΔCFS , (b) static ΔCFS , (c) peak slip, (d) peak slip rate, and (e) work per distance, W (Eq. (13)). All five parameters are estimated during the 15 seconds perturbation period. The ΔCFS values are measured at a depth corresponding to the maximum aseismic slip during the perturbation period in each simulation (i.e., z_{max}), while the other three parameters are measured along the entire fault. The Pearson correlation coefficient R is shown in the bottom right corner of each panel.

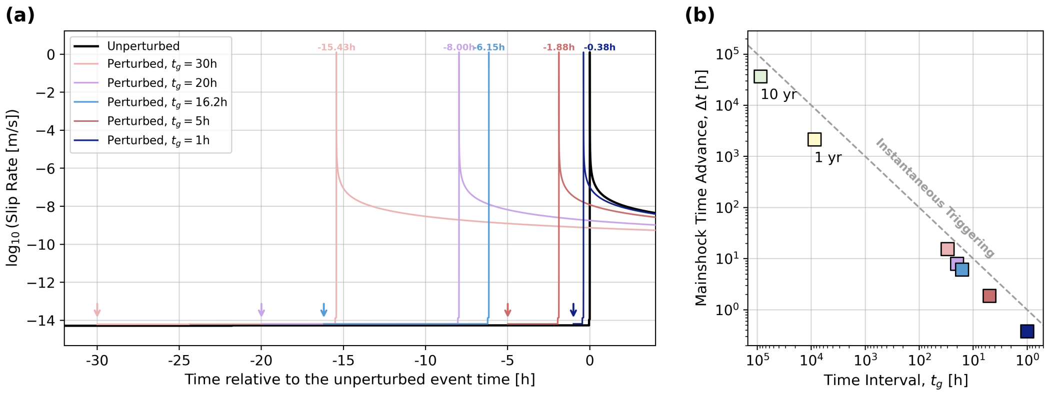

Figure 8. Comparison of triggering responses for different perturbation timings (t_g). (a) Slip rate at the mainshock hypocenter depth in the unperturbed model (4.38 km), for varying t_g values, ranging from 10 years (light green) to 1 hour (dark blue). Vertical arrows mark the timing of the applied dynamic perturbation for each t_g. (b) Relationship between the mainshock clock change (Δt) and the timing of perturbation. The grey dashed line indicates the expected Δt values for instantaneous triggering. Panels (a) and (b) share the same color scheme for each t_g. The example simulations shown here perturb target event 88 in the reference aging law seismic cycle model using the stress perturbation from the dynamic rupture model with a vertical foreshock fault, slow initiation (VSI), and a 340° strike orientation of the mainshock fault.

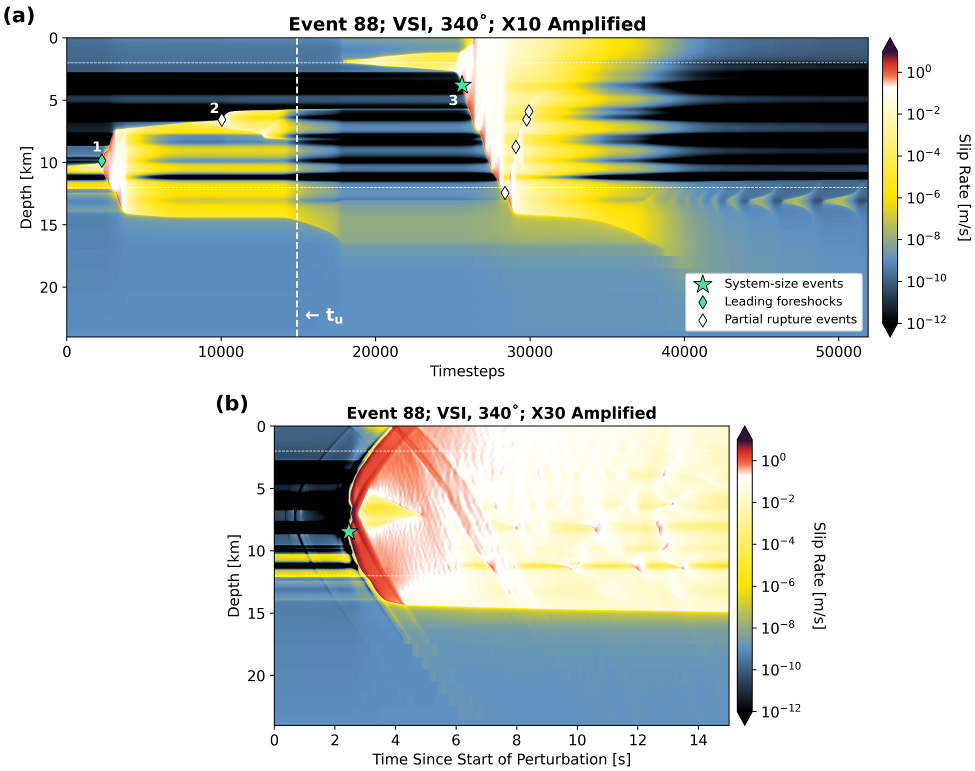

Figure 9. Spatiotemporal evolution of slip rate after applying stress perturbations with scaled amplitudes. (a) Result of the 10-times amplified stress model, where new events 1 and 2 occur 22 minutes and 1.6 hours after the initiation of the perturbation, respectively. A new system-size earthquake (new event 3) occurs approximately 74 days later than the target mainshock in the unperturbed model. (b) Result of the 30-times amplified stress model, where a system-size earthquake is triggered $\sim$ 2.5 seconds after the start of the perturbation. Green stars, green diamonds, and white diamonds indicate the hypocenter locations of system-size earthquakes, leading foreshocks, and partial rupture events, respectively. Both stress perturbation models are scaled versions of the stress perturbation from the dynamic rupture model with a vertical foreshock fault, slow initiation (VSI), and a 340° strike orientation of the mainshock fault.

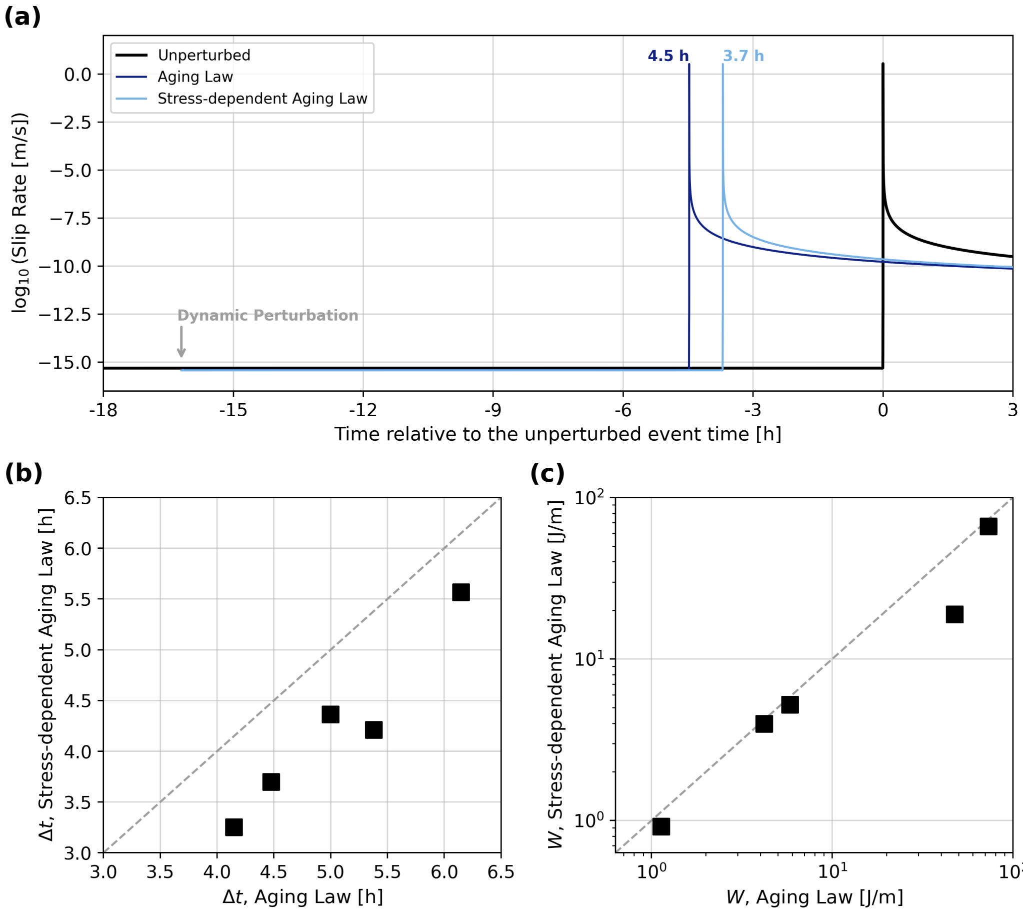

Figure 10. Comparison of seismic cycle models using the aging law (Eq. (9)) versus the stress-dependent aging law (Eq. (9) and Eq. (11)) during the perturbation period. (a) Slip rate at the mainshock hypocenter with the aging law (dark blue) and stress-dependent aging law (light blue). This example perturbs target event 282 (black) using a dynamic rupture model with vertical foreshock fault, slow initiation (VSI), and 340° strike orientation of the mainshock fault. (b-c) Comparison of the mainshock clock changes (Δt, panel b) and the work per distance values (W, panel c) produced by both models. The grey dashed line indicates a 1-to-1 relationship. Systematically smaller Δt and W values are obtained when using the stress-dependent aging law. The perturbation is applied to the aging law reference model for all explored cases.

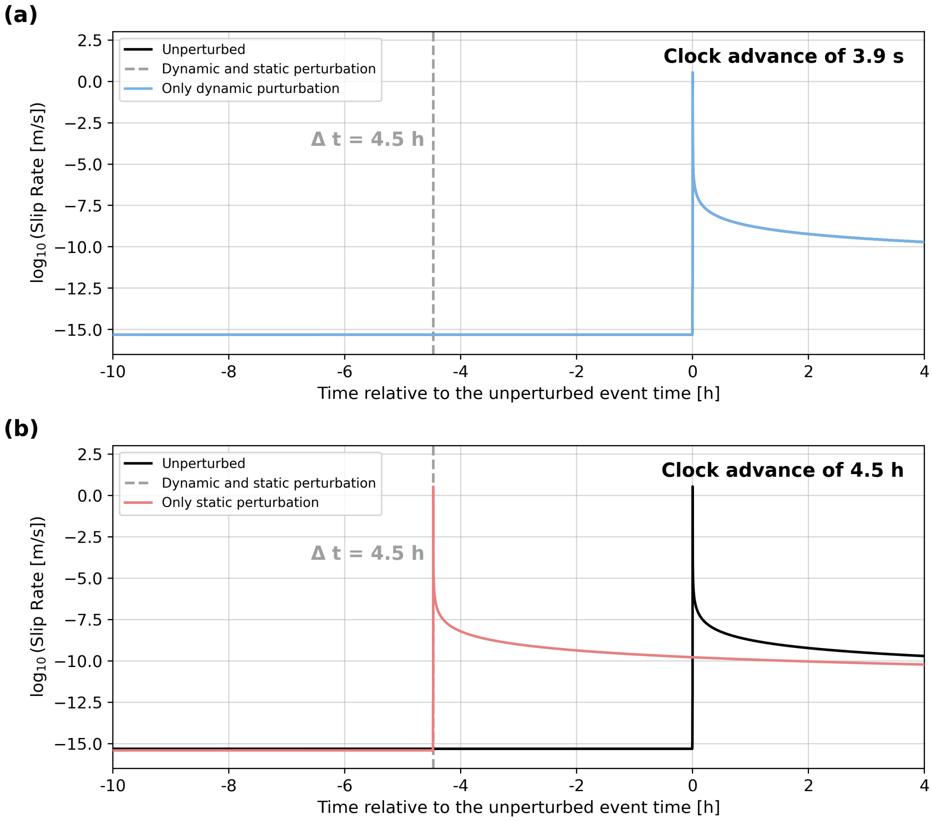

Figure 11. Comparison of the evolution of slip rate when perturbed by both dynamic and static components of ΔCFS (grey) with the slip rate when perturbed by (a) only the dynamic component of ΔCFS (see Fig. S8a) and (b) only the static component of ΔCFS (see Fig. S8b). The black line in both panels shows the slip rate evolution of the reference model (target mainshock event 282, 7.82 km depth). Note the similarity between the clock advances obtained from the static-only perturbation model (pink) and the full (both dynamic and static) perturbation model (grey).

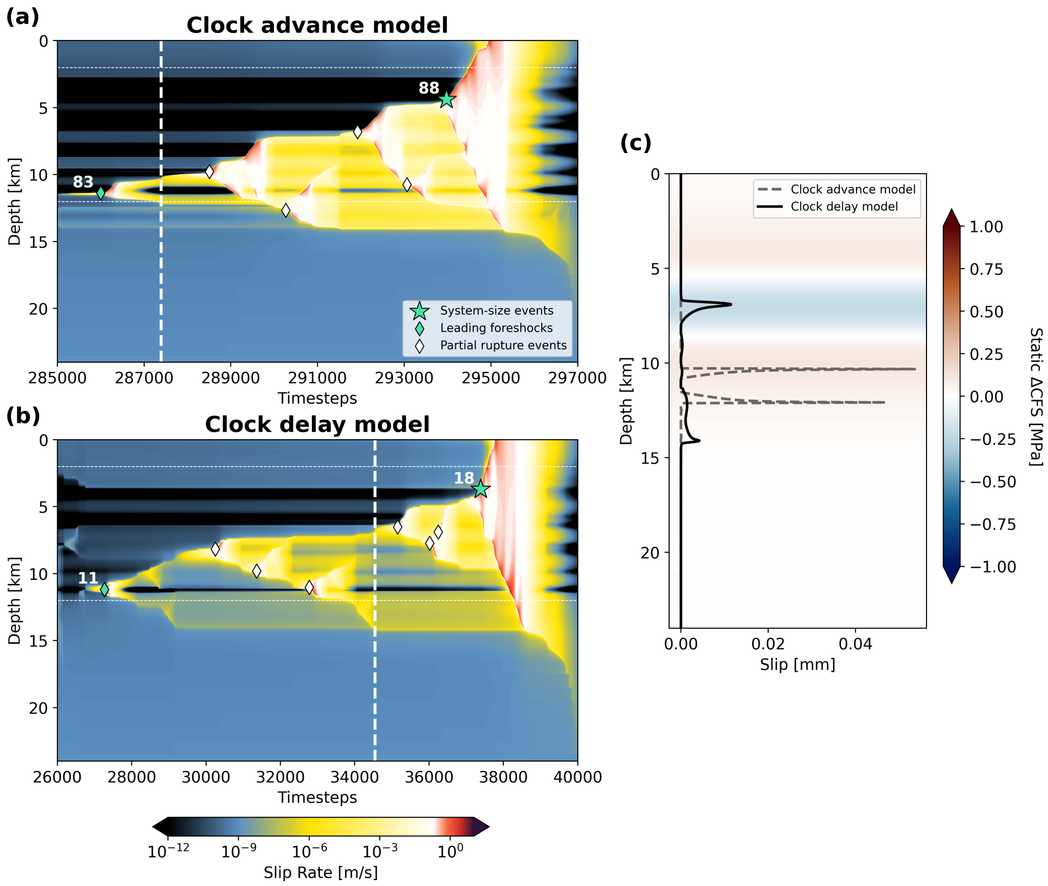

Figure 12. Comparison of the spatiotemporal evolution of slip rate for models with (a) mainshock clock advance (aging law reference model; target mainshock event 88) and (b) mainshock clock delay (A10 model; target mainshock event 18). Both models are perturbed using the same stress perturbation (VSI, 340° strike mainshock fault orientation). The white dashed line in both panels indicates the time when the dynamic perturbation is applied. Green stars, green diamonds, and white diamonds indicate the hypocenter locations of system-size earthquakes, leading foreshocks, and partial rupture events, respectively. (c) Net slip during the perturbation period for the clock advance (dashed lines) and clock delay (solid) models overlaying the static ΔCFS along the entire fault. In the clock advance model, the maximum slip during the perturbation period occurs predominantly under positive static ΔCFS , while in the clock delay model, it occurs predominantly in the static stress shadow. (VSI: vertical foreshock fault, slow initiation.)

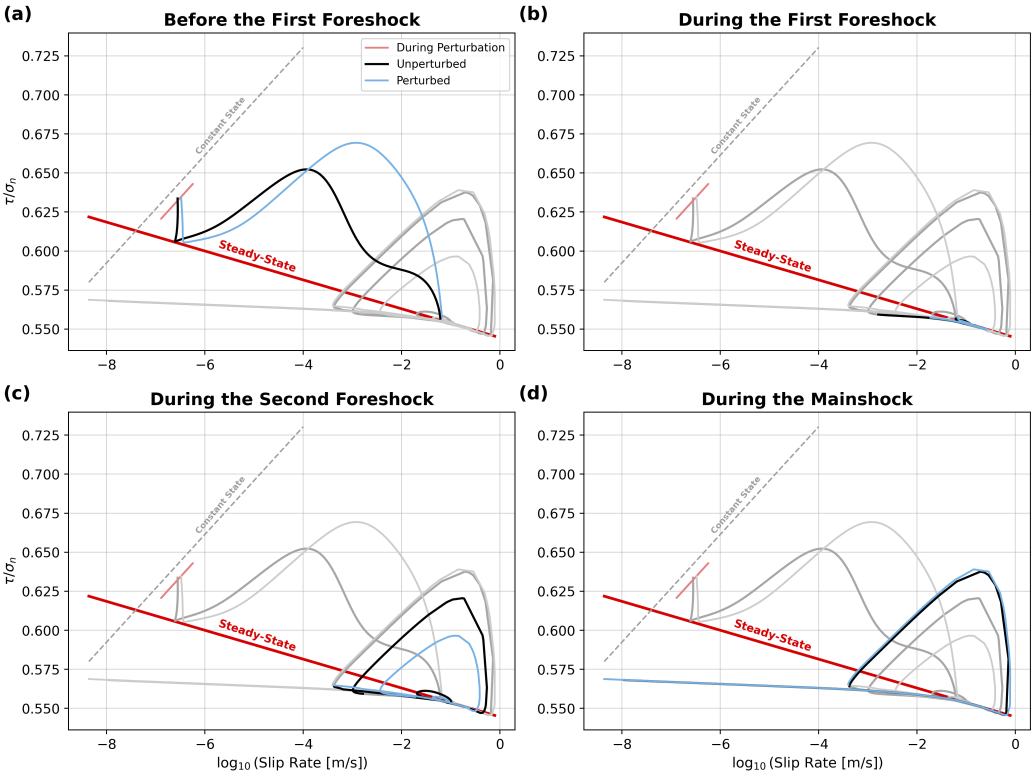

Figure 13. Phase diagram comparing the evolution of friction (shear stress over normal stress) as a function of slip rate for unperturbed model (black) and perturbed model (blue). The scenario perturbs event 282 (Fig. 6a) in the aging law reference model using the stress perturbation from the dynamic rupture model with a vertical foreshock fault, slow initiation (VSI), and a 340° strike orientation of the mainshock fault. For clarity, the diagram is divided into four stages: (a) before the first foreshock when shallow SSEs are dominant, (b) during the first foreshock (event 280 in Fig. 6a), (c) during the second foreshock (event 281 in Fig. 6a), and (d) during the system-size earthquake (i.e., mainshock, event 282 in Fig. 6a). The red solid line indicates the steady state, and the grey dashed line indicates the constant state variable contour. The incomplete cycle in panel (a) represents the shallow SSEs preceding the foreshock-mainshock sequence while panels (b) through (d) show well-developed limiting cycles of each earthquake. Friction and slip rate are measured at a depth corresponding to the maximum aseismic slip during the perturbation period ($z_{max} = 3.44$ km).

6 Open Research

All data required for reproducing the *SeisSol* dynamic rupture models and *Tandem* seismic cycle models can be downloaded from the Zenodo repository, `https://tinyurl.com/yaxbyc6z`. The open-source software *SeisSol* is available at `https://github.com/SeisSol/SeisSol`. We use *SeisSol* commit tag #e6ef661 in the master branch. The open-source software *Tandem* is available at `https://github.com/TEAR-ERC/tandem`. We use dmay/seas-checkpoint branch (commit #1dc36db; `https://github.com/TEAR-ERC/tandem/tree/dmay/seas-checkpoint`) for aging law simulations and jyun/state-law branch (commit #5d5c63f; `https://github.com/TEAR-ERC/tandem/tree/jyun/state_laws`) for slip law simulations. The location, timing, and focal mechanism of the 2019 Ridgecrest M_w 7.1 and M_w 5.4 earthquakes are retrieved from the U.S. Geological Survey Advanced National Seismic System Comprehensive Earthquake Catalog (ANSS ComCat) webpage (USGS, 2017, last accessed on 25 Aug, 2024).

Acknowledgments

We thank Prithvi Thakur, Camilla Cattania, and Junle Jiang for sharing their seismic cycle codes. We appreciate fruitful discussions with Eric Dunham, including the phase diagram analysis. YF acknowledges support from NSF (EAR-1841273) and NASA (80NSSC22K0506). AAG and DAM acknowledge support from NSF, grants EAR-2121568 (MTMOD) and OAC-2311208 (Quakeworx). AAG acknowledges support from NSF, grants OAC-2139536 (LCCF-CSA) and EAR-2225286, the Southern California Earthquake Center (SCEC awards 24103, 24127, 22135, 23121, 22162), the European Union's Horizon 2020 Research and Innovation Programme (TEAR, grant number 852992), Horizon Europe (ChEESE-2P, grant number 101093038, DT-GEO, grant number 101058129, and Geo-INQUIRE, grant number 101058518), and NASA (80NSSC20K0495). We gratefully acknowledge the computing resources provided by the Institute of Geophysics of LMU Munich (Oeser et al., 2006). We also acknowledge the Gauss Center for Supercomputing e.V. (`https://www.gauss-centre.eu/`) for providing computing time on SuperMUC-NG, hosted at the Leibniz Supercomputing Center (`https://www.lrz.de/`), via project pn49ha.

References

Abhyankar, S., Brown, J., Constantinescu, E., Ghosh, D., & Smith, B. F. (2014). *PETSc/TS: A modern scalable DAE/ODE solver library* (Preprint No. ANL/MCS-P5061-0114). Argonne National Laboratory.

Ader, T. J., Lapusta, N., Avouac, J.-P., & Ampuero, J.-P. (2014). Response of rate-and-state seismogenic faults to harmonic shear-stress perturbations. *Geophysical Journal International*, *198*(1), 385–413.

Aiken, C., & Peng, Z. (2014). Dynamic triggering of microearthquakes in three geothermal/volcanic regions of California. *Journal of Geophysical Research: Solid Earth*, *119*(9), 6992–7009.

Amestoy, P. R., Duff, I. S., L'Excellent, J.-Y., & Koster, J. (2001). A fully asynchronous multifrontal solver using distributed dynamic scheduling. *SIAM Journal on Matrix Analysis and Applications*, *23*(1), 15–41.

Amestoy, P. R., Guermouche, A., L'Excellent, J.-Y., & Pralet, S. (2006). Hybrid scheduling for the parallel solution of linear systems. *Parallel Computing*, *32*(2), 136–156.

Amos, C. B., Brownlee, S. J., Rood, D. H., Fisher, G. B., Bürgmann, R., Renne, P. R., & Jayko, A. S. (2013). Chronology of tectonic, geomorphic, and volcanic interactions and the tempo of fault slip near Little Lake, California. *Bulletin*, *125*(7-8), 1187–1202.

Ampuero, J.-P., & Rubin, A. M. (2008). Earthquake nucleation on rate and state faults – Aging and slip laws. *Journal of Geophysical Research: Solid Earth*, *113*(B1).

Andrews, D. (1976). Rupture velocity of plane strain shear cracks. *Journal of Geophysical Research*, *81*(32), 5679–5687.
Andrews, D., & Barall, M. (2011). Specifying initial stress for dynamic heterogeneous earthquake source models. *Bulletin of the Seismological Society of America*, *101*(5), 2408–2417.
Árnadóttir, T., Geirsson, H., & Einarsson, P. (2004). Coseismic stress changes and crustal deformation on the Reykjanes Peninsula due to triggered earthquakes on 17 June 2000. *Journal of Geophysical Research: Solid Earth*, *109*(B9).
Atkinson, B. K. (1984). Subcritical crack growth in geological materials. *Journal of Geophysical Research: Solid Earth*, *89*(B6), 4077–4114.
Balay, S., Abhyankar, S., Adams, M. F., Brown, J., Brune, P., Buschelman, K., ... Zhang, H. (2019). *PETSc users manual* (Tech. Rep. No. ANL-95/11 - Revision 3.11). Argonne National Laboratory.
Balay, S., Gropp, W. D., McInnes, L. C., & Smith, B. F. (1997). Efficient management of parallelism in object oriented numerical software libraries. In E. Arge, A. M. Bruaset, & H. P. Langtangen (Eds.), *Modern software tools in scientific computing* (pp. 163–202). Birkhäuser Press.
Barbot, S. (2019). Slow-slip, slow earthquakes, period-two cycles, full and partial ruptures, and deterministic chaos in a single asperity fault. *Tectonophysics*, *768*, 228171.
Belardinelli, M. E., Bizzarri, A., & Cocco, M. (2003). Earthquake triggering by static and dynamic stress changes. *Journal of Geophysical Research: Solid Earth*, *108*(B3).
Belardinelli, M. E., Cocco, M., Coutant, O., & Cotton, F. (1999). Redistribution of dynamic stress during coseismic ruptures: Evidence for fault interaction and earthquake triggering. *Journal of Geophysical Research: Solid Earth*, *104*(B7), 14925–14945.
Beroza, G. C., & Ide, S. (2011). Slow earthquakes and nonvolcanic tremor. *Annual review of Earth and planetary sciences*, *39*(1), 271–296.
Biemiller, J., Gabriel, A.-A., & Ulrich, T. (2022). The dynamics of unlikely slip: 3D modeling of low-angle normal fault rupture at the Mai'iu fault, Papua New Guinea. *Geochemistry, Geophysics, Geosystems*, *23*(5), e2021GC010298.
Boettcher, M., & Marone, C. (2004). Effects of normal stress variation on the strength and stability of creeping faults. *Journal of Geophysical Research: Solid Earth*, *109*(B3).
Bosl, W., & Nur, A. (2002). Aftershocks and pore fluid diffusion following the 1992 Landers earthquake. *Journal of Geophysical Research: Solid Earth*, *107*(B12), ESE–17.
Brodsky, E. E., & Prejean, S. G. (2005). New constraints on mechanisms of remotely triggered seismicity at Long Valley Caldera. *Journal of Geophysical Research: Solid Earth*, *110*(B4).
Brodsky, E. E., Roeloffs, E., Woodcock, D., Gall, I., & Manga, M. (2003). A mechanism for sustained groundwater pressure changes induced by distant earthquakes. *Journal of Geophysical Research: Solid Earth*, *108*(B8).
Caskey, S., & Wesnousky, S. (1997). Static stress changes and earthquake triggering during the 1954 Fairview Peak and Dixie Valley earthquakes, central Nevada. *Bulletin of the Seismological Society of America*, *87*(3), 521–527.
Cattania, C. (2019). Complex earthquake sequences on simple faults. *Geophysical Research Letters*, *46*(17-18), 10384–10393.
Cattania, C., & Segall, P. (2021). Precursory slow slip and foreshocks on rough faults. *Journal of Geophysical Research: Solid Earth*, *126*(4), e2020JB020430.
Chen, K. H., Nadeau, R. M., & Rau, R.-J. (2007). Towards a universal rule on the recurrence interval scaling of repeating earthquakes? *Geophysical Research Letters*, *34*(16).
Day, S. M., Dalguer, L. A., Lapusta, N., & Liu, Y. (2005). Comparison of finite

difference and boundary integral solutions to three-dimensional spontaneous rupture. *Journal of Geophysical Research: Solid Earth*, *110*(B12).

DeSalvio, N. D., & Fan, W. (2023). Ubiquitous earthquake dynamic triggering in southern California. *Journal of Geophysical Research: Solid Earth*, *128*(6), e2023JB026487.

Dieterich, J. H. (1979). Modeling of rock friction: 1. Experimental results and constitutive equations. *Journal of Geophysical Research: Solid Earth*, *84*(B5), 2161–2168.

Dieterich, J. H. (1994). A constitutive law for rate of earthquake production and its application to earthquake clustering. *Journal of Geophysical Research: Solid Earth*, *99*(B2), 2601–2618.

Dieterich, J. H., & Kilgore. (1994). Direct observation of frictional contacts: New insights for state-dependent properties. *Pure and applied geophysics*, *143*, 283–302.

Dong, P., Chen, R., Xia, K., Yao, W., Peng, Z., & Elsworth, D. (2022). Earthquake delay and rupture velocity in near-field dynamic triggering dictated by stress-controlled nucleation. *Seismological Research Letters*, *94*(2A), 913-924.

Dublanchet, P., Bernard, P., & Favreau, P. (2013). Creep modulation of Omori law generated by a Coulomb stress perturbation in a 3-D rate-and-state asperity model. *Journal of Geophysical Research: Solid Earth*, *118*(9), 4774–4793.

Dumbser, M., & Käser, M. (2006). An arbitrary high-order discontinuous Galerkin method for elastic waves on unstructured meshes—II. The three-dimensional isotropic case. *Geophysical Journal International*, *167*(1), 319–336.

Dunham, E. M., Belanger, D., Cong, L., & Kozdon, J. E. (2011). Earthquake ruptures with strongly rate-weakening friction and off-fault plasticity, part 2: Nonplanar faults. *Bulletin of the Seismological Society of America*, *101*(5), 2308–2322.

Elkhoury, J. E., Brodsky, E. E., & Agnew, D. C. (2006). Seismic waves increase permeability. *Nature*, *441*(7097), 1135–1138.

Erickson, B. A., & Dunham, E. M. (2014). An efficient numerical method for earthquake cycles in heterogeneous media: Alternating subbasin and surface-rupturing events on faults crossing a sedimentary basin. *Journal of Geophysical Research: Solid Earth*, *119*(4), 3290–3316.

Farain, K., & Bonn, D. (2024). Perturbation-induced granular fluidization as a model for remote earthquake triggering. *Science Advances*, *10*(16), eadi7302.

Felzer, K. R., & Brodsky, E. E. (2005). Testing the stress shadow hypothesis. *Journal of Geophysical Research: Solid Earth*, *110*(B5).

Felzer, K. R., & Brodsky, E. E. (2006). Decay of aftershock density with distance indicates triggering by dynamic stress. *Nature*, *441*(7094), 735–738.

Freed, A. M. (2005). Earthquake triggering by static, dynamic, and postseismic stress transfer. *Annu. Rev. Earth Planet. Sci.*, *33*, 335–367.

Gabriel, A.-A., Garagash, D. I., Palgunadi, K. H., & Mai, P. M. (2024). Fault size–dependent fracture energy explains multiscale seismicity and cascading earthquakes. *Science*, *385*(6707), eadj9587.

Gabriel, A.-A., Ulrich, T., Marchandon, M., Biemiller, J., & Rekoske, J. (2023). 3D Dynamic Rupture Modeling of the 6 February 2023, Kahramanmaraş, Turkey M_w 7.8 and 7.7 Earthquake Doublet Using Early Observations. *The Seismic Record*, *3*(4), 342–356.

Gallovič, F. (2008). Heterogeneous Coulomb stress perturbation during earthquake cycles in a 3D rate-and-state fault model. *Geophysical research letters*, *35*(21).

Galvez, P., Somerville, P., Petukhin, A., Ampuero, J.-P., & Peter, D. (2020). Earthquake cycle modelling of multi-segmented faults: dynamic rupture and ground motion simulation of the 1992 M_w 7.3 Landers earthquake. *Pure and Applied Geophysics*, *177*, 2163–2179.

Gomberg, J. (1996). Stress/strain changes and triggered seismicity following the

M_w 7.3 Landers, California earthquake. *Journal of Geophysical Research: Solid Earth*, *101*(B1), 751–764.

Gomberg, J., Beeler, N., Blanpied, M., & Bodin, P. (1998). Earthquake triggering by transient and static deformations. *Journal of Geophysical Research: Solid Earth*, *103*(B10), 24411–24426.

Gomberg, J., Blanpied, M. L., & Beeler, N. (1997). Transient triggering of near and distant earthquakes. *Bulletin of the Seismological Society of America*, *87*(2), 294–309.

Gomberg, J., Reasenberg, P., Bodin, P. l., & Harris, R. (2001). Earthquake triggering by seismic waves following the Landers and Hector Mine earthquakes. *Nature*, *411*(6836), 462–466.

Guo, H., Brodsky, E. E., & Miyazawa, M. (2024). Triggering Intensity Changes over Time and Space as Measured by Continuous Waveforms in southern California. *ESS Open Archive eprints*, *867*, 172222568–86733850.

Hardebeck, J. L., & Harris, R. A. (2022). Earthquakes in the shadows: Why aftershocks occur at surprising locations. *The Seismic Record*, *2*(3), 207–216.

Harris, R. A., & Simpson, R. W. (1992). Changes in static stress on southern California faults after the 1992 Landers earthquake. *Nature*, *360*(6401), 251–254.

Hauksson, E., & Jones, L. M. (2020). Seismicity, stress state, and style of faulting of the Ridgecrest-Coso region from the 1930s to 2019: Seismotectonics of an evolving plate boundary segment. *Bulletin of the Seismological Society of America*, *110*(4), 1457–1473.

Heinecke, A., Breuer, A., Rettenberger, S., Bader, M., Gabriel, A.-A., Pelties, C., . . . others (2014). Petascale high order dynamic rupture earthquake simulations on heterogeneous supercomputers. In *Sc'14: Proceedings of the international conference for high performance computing, networking, storage and analysis* (pp. 3–14).

Hill, D. P., & Prejean, S. (2015). 4.11 - Dynamic Triggering. In G. Schubert (Ed.), *Treatise on geophysics (second edition)* (Second Edition ed., p. 273-304). Oxford: Elsevier. doi: https://doi.org/10.1016/B978-0-444-53802-4.00078-6

Hill, D. P., Reasenberg, P., Michael, A., Arabaz, W., Beroza, G., Brumbaugh, D., . . . others (1993). Seismicity remotely triggered by the magnitude 7.3 Landers, California, earthquake. *Science*, *260*(5114), 1617–1623.

Hillers, G., Mai, P., Ben-Zion, Y., & Ampuero, J.-P. (2007). Statistical properties of seismicity of fault zones at different evolutionary stages. *Geophysical Journal International*, *169*(2), 515–533.

Hirose, F., Miyaoka, K., Hayashimoto, N., Yamazaki, T., & Nakamura, M. (2011). Outline of the 2011 off the Pacific coast of Tohoku Earthquake (M_w 9.0) - Seismicity: foreshocks, mainshock, aftershocks, and induced activity -. *Earth, planets and space*, *63*, 513–518.

Hudnut, K. W., Seeber, L., & Pacheco, J. (1989). Cross-fault triggering in the November 1987 Superstition Hills earthquake sequence, southern California. *Geophysical Research Letters*, *16*(2), 199–202.

Husen, S., Wiemer, S., & Smith, R. B. (2004). Remotely triggered seismicity in the Yellowstone National Park region by the 2002 M_w 7.9 Denali fault earthquake, Alaska. *Bulletin of the Seismological Society of America*, *94*(6B), S317–S331.

Ida, Y. (1972). Cohesive force across the tip of a longitudinal-shear crack and Griffith's specific surface energy. *Journal of Geophysical Research*, *77*(20), 3796–3805.

Inbal, A., Ziv, A., Lior, I., Nof, R. N., & Eisermann, A. S. (2023). Non-triggering and then triggering of a repeating aftershock sequence in the Dead Sea by the 2023 Kahramanmaraş Earthquake pair: Implications for the physics of remote delayed aftershocks. *Geophysical Research Letters*, *50*(18), e2023GL104908.

Jia, Z., Jin, Z., Marchandon, M., Ulrich, T., Gabriel, A.-A., Fan, W., . . . others (2023). The complex dynamics of the 2023 Kahramanmaraş, Turkey, M_w

7.8-7.7 earthquake doublet. *Science*, *381*(6661), 985–990.

Jia, Z., Wang, X., & Zhan, Z. (2020). Multifault models of the 2019 Ridgecrest sequence highlight complementary slip and fault junction instability. *Geophysical Research Letters*, *47*(17), e2020GL089802.

Jiang, J., & Fialko, Y. (2016). Reconciling seismicity and geodetic locking depths on the Anza section of the San Jacinto fault. *Geophys. Res. Lett.*, *43*(20), 10663–10671.

Jin, Y., Dyaur, N., & Zheng, Y. (2021). Laboratory evidence of transient pressure surge in a fluid-filled fracture as a potential driver of remote dynamic earthquake triggering. *The Seismic Record*, *1*(2), 66–74.

Jin, Z., & Fialko, Y. (2020). Finite slip models of the 2019 Ridgecrest earthquake sequence constrained by space geodetic data and aftershock locations. *Bulletin of the Seismological Society of America*, *110*(4), 1660–1679.

Johnson, P. A., & Jia, X. (2005). Nonlinear dynamics, granular media and dynamic earthquake triggering. *Nature*, *437*(7060), 871–874.

Kaneko, Y., & Lapusta, N. (2008). Variability of earthquake nucleation in continuum models of rate-and-state faults and implications for aftershock rates. *Journal of Geophysical Research: Solid Earth*, *113*(B12).

Katakami, S., Kaneko, Y., Ito, Y., & Araki, E. (2020). Stress sensitivity of instantaneous dynamic triggering of shallow slow slip events. *Journal of Geophysical Research: Solid Earth*, *125*(6), e2019JB019178.

Kilb, D., Gomberg, J., & Bodin, P. (2000). Triggering of earthquake aftershocks by dynamic stresses. *Nature*, *408*(6812), 570–574.

King, G. C., Stein, R. S., & Lin, J. (1994). Static stress changes and the triggering of earthquakes. *Bulletin of the Seismological Society of America*, *84*(3), 935–953.

Kostka, F., & Gallovič, F. (2016). Static Coulomb stress load on a three-dimensional rate-and-state fault: Possible explanation of the anomalous delay of the 2004 Parkfield earthquake. *Journal of Geophysical Research: Solid Earth*, *121*(5), 3517–3533.

Krenz, L., Uphoff, C., Ulrich, T., Gabriel, A.-A., Abrahams, L. S., Dunham, E. M., & Bader, M. (2021). 3D acoustic-elastic coupling with gravity: the dynamics of the 2018 Palu, Sulawesi earthquake and tsunami. In *Proceedings of the international conference for high performance computing, networking, storage and analysis* (pp. 1–14).

Kroll, K. A., Dieterich, J. H., Richards-Dinger, K. B., & Oglesby, D. D. (2023). 3-D Simulations of earthquakes rupture jumps: 1. Homogeneous pre-stress conditions. *Geophysical Journal International*, *234*(1), 395–403.

Kroll, K. A., Richards-Dinger, K. B., Dieterich, J. H., & Cochran, E. S. (2017). Delayed seismicity rate changes controlled by static stress transfer. *Journal of Geophysical Research: Solid Earth*, *122*(10), 7951–7965.

Lapusta, N., Rice, J. R., Ben-Zion, Y., & Zheng, G. (2000). Elastodynamic analysis for slow tectonic loading with spontaneous rupture episodes on faults with rate-and state-dependent friction. *Journal of Geophysical Research: Solid Earth*, *105*(B10), 23765–23789.

Lee, E.-J., Chen, P., Jordan, T. H., Maechling, P. J., Denolle, M. A., & Beroza, G. C. (2014). Full-3-D tomography for crustal structure in southern California based on the scattering-integral and the adjoint-wavefield methods. *Journal of Geophysical Research: Solid Earth*, *119*(8), 6421–6451.

Lee, J.-J., & Bruhn, R. L. (1996). Structural anisotropy of normal fault surfaces. *Journal of Structural Geology*, *18*(8), 1043–1059.

Li, D., & Gabriel, A.-A. (2024). Linking 3D long-term slow-slip cycle models with rupture dynamics: The nucleation of the 2014 M_w 7.3 Guerrero, Mexico earthquake. *AGU Advances*, *5*(2), e2023AV000979.

Linde, A. T., Suyehiro, K., Miura, S., Sacks, I. S., & Takagi, A. (1988). Episodic aseismic earthquake precursors. *Nature*, *334* (6182), 513–515.

Lindsey, E. O., & Fialko, Y. (2016). Geodetic constraints on frictional properties and earthquake hazard in the Imperial Valley, Southern California. *Journal of Geophysical Research: Solid Earth*, *121*, 1097–1113.

Linker, M., & Dieterich, J. H. (1992). Effects of variable normal stress on rock friction: Observations and constitutive equations. *Journal of Geophysical Research: Solid Earth*, *97* (B4), 4923–4940.

Liu, D., Duan, B., & Luo, B. (2020). EQsimu: a 3-D finite element dynamic earthquake simulator for multicycle dynamics of geometrically complex faults governed by rate-and state-dependent friction. *Geophysical Journal International*, *220* (1), 598–609.

Luo, Y., & Ampuero, J.-P. (2018). Stability of faults with heterogeneous friction properties and effective normal stress. *Tectonophysics*, *733*, 257–272.

Luo, Y., & Liu, Z. (2019). Slow-slip recurrent pattern changes: Perturbation responding and possible scenarios of precursor toward a megathrust earthquake. *Geochemistry, Geophysics, Geosystems*, *20* (2), 852–871.

Meng, H., & Fan, W. (2021). Immediate foreshocks indicating cascading rupture developments for 527 M 0.9 to 5.4 Ridgecrest earthquakes. *Geophysical Research Letters*, *48* (19), e2021GL095704.

Nadeau, R. M., & Johnson, L. R. (1998). Seismological studies at Parkfield VI: Moment release rates and estimates of source parameters for small repeating earthquakes. *Bulletin of the Seismological Society of America*, *88* (3), 790–814.

Noda, H., Dunham, E. M., & Rice, J. R. (2009). Earthquake ruptures with thermal weakening and the operation of major faults at low overall stress levels. *Journal of Geophysical Research: Solid Earth*, *114* (B7).

Oeser, J., Bunge, H.-P., & Mohr, M. (2006). Cluster design in the earth sciences tethys. In *International conference on high performance computing and communications* (pp. 31–40).

Palmer, A. C., & Rice, J. R. (1973). The growth of slip surfaces in the progressive failure of over-consolidated clay. *Proceedings of the Royal Society of London. A. Mathematical and Physical Sciences*, *332* (1591), 527–548.

Parsons, T. (2005). A hypothesis for delayed dynamic earthquake triggering. *Geophysical Research Letters*, *32* (4).

Parsons, T., & Dreger, D. S. (2000). Static-stress impact of the 1992 Landers earthquake sequence on nucleation and slip at the site of the 1999 M= 7.1 Hector Mine earthquake, southern California. *Geophysical research letters*, *27* (13), 1949–1952.

Pelties, C., Gabriel, A.-A., & Ampuero, J.-P. (2014). Verification of an ADER-DG method for complex dynamic rupture problems. *Geoscientific Model Development*, *7* (3), 847–866.

Perfettini, H., Schmittbuhl, J., & Cochard, A. (2003a). Shear and normal load perturbations on a two-dimensional continuous fault: 1. Static triggering. *Journal of Geophysical Research: Solid Earth*, *108* (B9).

Perfettini, H., Schmittbuhl, J., & Cochard, A. (2003b). Shear and normal load perturbations on a two-dimensional continuous fault: 2. Dynamic triggering. *Journal of Geophysical Research: Solid Earth*, *108* (B9).

Perfettini, H., Schmittbuhl, J., Rice, J. R., & Cocco, M. (2001). Frictional response induced by time-dependent fluctuations of the normal loading. *Journal of Geophysical Research: Solid Earth*, *106* (B7), 13455–13472.

Pignalberi, F., Giorgetti, C., Noël, C., Marone, C., Collettini, C., & Scuderi, M. M. (2024). The effect of normal stress oscillations on fault slip behavior near the stability transition from stable to unstable motion. *Journal of Geophysical Research: Solid Earth*, *129* (2), e2023JB027470.

Pranger, C. C. (2020). *Unstable physical processes operating on self-governing fault systems, improved modeling methodology* (Unpublished doctoral dissertation).

ETH Zurich.

Pranger, C. C., Sanan, P., May, D. A., Le Pourhiet, L., & Gabriel, A.-A. (2022). Rate and state friction as a spatially regularized transient viscous flow law. *Journal of Geophysical Research: Solid Earth*, *127*(6), e2021JB023511.

Ramos, M. D., Thakur, P., Huang, Y., Harris, R. A., & Ryan, K. J. (2022). Working with dynamic earthquake rupture models: A practical guide. *Seismological Society of America*, *93*(4), 2096–2110.

Renard, F., & Candela, T. (2017). Scaling of fault roughness and implications for earthquake mechanics. *Fault zone dynamic processes: Evolution of fault properties during seismic rupture*, 195–215.

Renard, F., Voisin, C., Marsan, D., & Schmittbuhl, J. (2006). High resolution 3D laser scanner measurements of a strike-slip fault quantify its morphological anisotropy at all scales. *Geophysical Research Letters*, *33*(4).

Rice, J. R. (1993). Spatio-temporal complexity of slip on a fault. *Journal of Geophysical Research: Solid Earth*, *98*(B6), 9885–9907.

Rice, J. R., & Ben-Zion, Y. (1996). Slip complexity in earthquake fault models. *Proceedings of the National Academy of Sciences*, *93*(9), 3811–3818.

Rice, J. R., & Tse, S. T. (1986). Dynamic motion of a single degree of freedom system following a rate and state dependent friction law. *Journal of Geophysical Research: Solid Earth*, *91*(B1), 521–530.

Richardson, E., & Marone, C. (1999). Effects of normal stress vibrations on frictional healing. *Journal of Geophysical Research: Solid Earth*, *104*(B12), 28859–28878.

Ross, Z. E., Idini, B., Jia, Z., Stephenson, O. L., Zhong, M., Wang, X., ... others (2019). Hierarchical interlocked orthogonal faulting in the 2019 Ridgecrest earthquake sequence. *Science*, *366*(6463), 346–351.

Rousset, B., Bürgmann, R., & Campillo, M. (2019). Slow slip events in the roots of the San Andreas fault. *Science advances*, *5*(2), eaav3274.

Rubin, A. M. (2008). Episodic slow slip events and rate-and-state friction. *Journal of Geophysical Research: Solid Earth*, *113*(B11).

Ruina, A. (1983). Slip instability and state variable friction laws. *Journal of Geophysical Research: Solid Earth*, *88*(B12), 10359–10370.

SCEDC. (2013). *Southern California Earthquake Data Center.* Caltech. Retrieved from `http://scedc.caltech.edu` doi: 10.7909/C3WD3XH1

Shelly, D. R. (2020). A high-resolution seismic catalog for the initial 2019 Ridgecrest earthquake sequence: Foreshocks, aftershocks, and faulting complexity. *Seismological Research Letters*, *91*(4), 1971–1978.

Shelly, D. R., Peng, Z., Hill, D. P., & Aiken, C. (2011). Triggered creep as a possible mechanism for delayed dynamic triggering of tremor and earthquakes. *Nature Geoscience*, *4*(6), 384–388.

Shi, Z., & Day, S. M. (2013). Rupture dynamics and ground motion from 3-D rough-fault simulations. *Journal of Geophysical Research: Solid Earth*, *118*(3), 1122–1141.

Small, P. E., Gill, D., Maechling, P. J., Taborda, R., Callaghan, S., Jordan, T. H., ... Goulet, C. (2017). The SCEC unified community velocity model software framework. *Seismological Research Letters*, *88*(6), 1539–1552.

Small, P. E., Maechling, P. J., & Su, M.-H. (2022). *The Unified Community Velocity Model (UCVM).* Zenodo. Retrieved from `https://doi.org/10.5281/zenodo.7033687` doi: 10.5281/zenodo.7033687

Stein, R. S. (1999). The role of stress transfer in earthquake occurrence. *Nature*, *402*(6762), 605–609.

Tal, Y., & Gabrieli, T. (2024). Dual effect of roughness during earthquake rupture sequences on faults with strongly rate-weakening friction. *Earth and Planetary Science Letters*, *637*, 118738.

Taufiqurrahman, T., Gabriel, A.-A., Li, D., Ulrich, T., Li, B., Carena, S., ...

Gallovič, F. (2023). Dynamics, interactions and delays of the 2019 Ridgecrest rupture sequence. *Nature*, *618*(7964), 308–315.

Thakur, P., Huang, Y., & Kaneko, Y. (2020). Effects of low-velocity fault damage zones on long-term earthquake behaviors on mature strike-slip faults. *Journal of Geophysical Research: Solid Earth*, *125*(8), e2020JB019587.

Thomas, M. Y., Lapusta, N., Noda, H., & Avouac, J.-P. (2014). Quasi-dynamic versus fully dynamic simulations of earthquakes and aseismic slip with and without enhanced coseismic weakening. *Journal of Geophysical Research: Solid Earth*, *119*(3), 1986–2004.

Thurber, C. H. (1996). Creep events preceding small to moderate earthquakes on the San Andreas fault. *Nature*, *380*(6573), 425–428.

Thurber, C. H., & Sessions, R. (1998). Assessment of creep events as potential earthquake precursors: application to the creeping section of the San Andreas fault, California. *pure and applied geophysics*, *152*, 685–705.

Toda, S., Stein, R. S., Beroza, G. C., & Marsan, D. (2012). Aftershocks halted by static stress shadows. *Nature Geoscience*, *5*(6), 410–413.

Turner, A., Hawthorne, J., & Cattania, C. (2024). Partial ruptures cannot explain the long recurrence intervals of repeating earthquakes. *Journal of Geophysical Research: Solid Earth*, *129*(1), e2023JB027870.

Tymofyeyeva, E., Fialko, Y., Jiang, J., Xu, X., Sandwell, D., Bilham, R., … others (2019). Slow slip event on the Southern San Andreas fault triggered by the 2017 M_w 8.2 Chiapas (Mexico) earthquake. *Journal of Geophysical Research: Solid Earth*, *124*(9), 9956–9975.

Uchida, N., & Bürgmann, R. (2019). Repeating earthquakes. *Annual Review of Earth and Planetary Sciences*, *47*(1), 305–332.

Ulrich, T., Gabriel, A.-A., Ampuero, J.-P., & Xu, W. (2019). Dynamic viability of the 2016 M_w 7.8 Kaikōura earthquake cascade on weak crustal faults. *Nature communications*, *10*(1), 1213.

Uphoff, C., May, D. A., & Gabriel, A.-A. (2023). A discontinuous Galerkin method for sequences of earthquakes and aseismic slip on multiple faults using unstructured curvilinear grids. *Geophysical Journal International*, *233*(1), 586–626.

Uphoff, C., Rettenberger, S., Bader, M., Madden, E. H., Ulrich, T., Wollherr, S., & Gabriel, A.-A. (2017). Extreme scale multi-physics simulations of the tsunamigenic 2004 Sumatra megathrust earthquake. In *Proceedings of the international conference for high performance computing, networking, storage and analysis* (pp. 1–16).

USGS. (2017). *Advanced National Seismic System (ANSS) Comprehensive Catalog.* U.S. Geological Survey. Retrieved from `http://earthquake.usgs.gov/earthquakes/search/` doi: 10.5066/F7MS3QZH

van der Elst, N. J., & Brodsky, E. E. (2010). Connecting near-field and far-field earthquake triggering to dynamic strain. *Journal of Geophysical Research: Solid Earth*, *115*(B7).

van der Elst, N. J., & Shaw, B. E. (2015). Larger aftershocks happen farther away: Nonseparability of magnitude and spatial distributions of aftershocks. *Geophysical Research Letters*, *42*(14), 5771–5778.

Wei, M., Kaneko, Y., Liu, Y., & McGuire, J. J. (2013). Episodic fault creep events in California controlled by shallow frictional heterogeneity. *Nature geoscience*, *6*(7), 566–570.

Wei, M., Kaneko, Y., Shi, P., & Liu, Y. (2018). Numerical modeling of dynamically triggered shallow slow slip events in New Zealand by the 2016 M_w 7.8 Kaikoura earthquake. *Geophysical Research Letters*, *45*(10), 4764–4772.

Wollherr, S., Gabriel, A.-A., & Uphoff, C. (2018). Off-fault plasticity in three-dimensional dynamic rupture simulations using a modal Discontinuous Galerkin method on unstructured meshes: implementation, verification and application. *Geophysical Journal International*, *214*(3), 1556–1584.

Yin, Y., Galvez, P., Heimisson, E. R., & Wiemer, S. (2023). The role of three-dimensional fault interactions in creating complex seismic sequences. *Earth and Planetary Science Letters*, *606*, 118056.

Yoshida, S., Maeda, T., & Kato, N. (2020). Earthquake triggering model based on normal-stress-dependent Nagata law: application to the 2016 Mie offshore earthquake. *Earth, Planets and Space*, *72*, 1–13.

Zhu, W., Allison, K. L., Dunham, E. M., & Yang, Y. (2020). Fault valving and pore pressure evolution in simulations of earthquake sequences and aseismic slip. *Nature communications*, *11*(1), 4833.

JOURNAL OF GEOPHYSICAL RESEARCH

Supporting Information for "Controls of Dynamic and Static Stress Changes and Aseismic Slip on Delayed Earthquake Triggering in Rate-and-State Simulations of the 2019 Ridgecrest Earthquake Sequence"

Jeena Yun[1], Alice-Agnes Gabriel[1,2], Dave A. May[1], and Yuri Fialko[1]

[1]Scripps Institution of Oceanography, University of California San Diego, La Jolla, CA, USA

[2]Department of Earth and Environmental Sciences, Ludwig-Maximilians Universität München, Munich, Germany

Contents of this file

Text S1. Numerical Resolution of Volumetric Discontinuous Galerkin Seismic Cycle Models with *Tandem*

We analyze the two most important length scales that need to be resolved in seismic cycle models: the process zone size (Λ_0) and the critical nucleation size (L_∞; Erickson et al., 2020; Jiang et al., 2022; Rice, 1993). The quasi-static process zone is the area near the rupture front where the fault dynamically weakens, which can be estimated as follows (Day et al., 2005):

$$\Lambda_0 = C\frac{\mu D_{RS}}{b\sigma_n}$$

with C being a constant of an order of 1. For 2D anti-plane simulations using the aging law (with $0.5 < a/b < 1$), the critical nucleation size can be expressed as follows (Rubin & Ampuero, 2005):

$$L_\infty = \frac{2}{\pi}\frac{\mu b D_{RS}}{\sigma_n(b-a)^2}. \tag{1}$$

Our aging law reference model has the smallest values for Λ_0 and L_∞ are 25.47 m and 39.83 m, respectively (Table 2).

Tandem is a volume-based discontinuous Galerkin code (Uphoff et al., 2023) and must discretize the 2D domain with sufficiently small elements to resolve both Λ_0 and L_∞. To ease computation, we use static gradual mesh coarsening, in which high resolution can be localized in a region around the fault. The minimum element size is prescribed at the fault.

The high-order basis function in *Tandem*'s discontinuous Galerkin scheme provides sub-element resolution, allowing larger element sizes compared to low-order methods without sacrificing accuracy (Uphoff et al., 2023). In this study, we use a basis function of polynomial degree 6 and take an on-fault (minimum) element size (Δz) of 25 m, resulting in an effective element size of ~ 4 m per degree of freedom. This model resolves the minimum length scale with 6 elements. Away from the fault, the element sizes gradually increase up to 50 km at boundaries.

To verify the effective resolution of the model, we compare this model with a higher resolution model using a smaller Δz of 10 m, resulting in the smallest effective element size of ~ 1.6 m. The two models evolve identically until ~ 150 years of simulation time. Afterward, minor deviations gradually accumulate (Fig. S15). These deviations are likely resulting from accumulated round-off errors over time. Since the problem is highly nonlinear, small round-off errors can lead to a visible deviation between equivalent models (i.e., Erickson et al., 2020). To reach 300 years of simulation time, the $\Delta z = 10$ m model takes 3 times more steps than the $\Delta z = 25$ m model, which potentially allows more round-off error to accrue.

Regardless of the minor difference between the two models, the characteristic complexities in the earthquake cycle (e.g., the cascade of partial ruptures, shallow and deep SSEs, and a range of hypocenter depths) spontaneously emerge in both models. The qualitative similarity implies that these complexities are not the artifacts observed in inherently discrete models induced by the oversized cells (Erickson et al., 2020; Rice, 1993; Rice & Ben-Zion, 1996).

We also test the robustness of our estimates of triggering response with a few representative cases. The main findings (e.g., several hours of time advance, mainshock clock advance when the work per distance $W > 0$) from the $\Delta z = 25$ m model are kept in the $\Delta z = 10$ m model. Thus, we conclude that $\Delta z = 25$ m is appropriately resolving the physics of the system while keeping the computational expense reasonable.

For slip law simulations, finer spatial resolution is required to properly resolve the nucleation size (Ampuero & Rubin, 2008). Ampuero and Rubin (2008) used a grid spacing of $L_b/50 - L_b/150$ in their simulations with the slip law, where $L_b = \mu D_{RS}/b\sigma_n$ (Dieterich, 1992). The slip law reference model ($\overline{D_{RS}} = 10$ m; see Section 3.2 in the main text) has minimum $L_b = 127$ m and we use $\Delta z = L_b/10 \approx 10$ m, resolving L_b with 76 elements. The A10 model (see Section 3.2 in the main text) uses Δz of 125 m, which is a factor of 5 larger than the aging law reference model, reflecting the difference in $\overline{D_{RS}}$.

Text S2. Low Rigidity Fault Zone

We performed additional seismic cycle simulations adding a low-rigidity region surrounding the fault, as an analogy to damage zones developing near active faults (e.g., Chester et al., 1993; Huang et al., 2014; Idini & Ampuero, 2020; Thakur et al., 2020). Thakur et al. (2020) showed that including a low-rigidity fault zone can introduce aperiodic earthquake sequences with a wide range of hypocenter depths in 2D fully dynamic strike-slip seismic cycle simulations. We include a rectangular low-rigidity zone, 500 m wide and 10 km deep, which tapers towards the fault at depth in a quarter-circle-shape with a 500 m radius (Fig. 2a in the main text). We explore two fault zone rigidity values (μ_{DZ}), 10 GPa and 20 GPa, corresponding to a higher and lower contrast to the bulk rigidity $\mu = 32$ GPa.

However, the low-rigidity fault zone has minimal impact on earthquake sequences within our considered model space, regardless of the rigidity contrast. Without the inclusion of fractal heterogeneities in the initial dynamic parameters, the low-rigidity zone alone results in partial ruptures and system-size earthquakes, but the sequence remains perfectly cycle-invariant with hypocenters located only at the bottom of the seismogenic zone. This cycle-invariant behavior may be attributed to the absence of complex wave interaction within the fault zone in our models as we approximate the inertial effect using the radiation damping term (Eq. (5) in the main text), while the fully elastodynamic scheme used in Thakur et al. (2020). When the low-rigidity fault zone ($\mu_{DZ} = 20$ GPa & $\mu = 32$ GPa) is included in the models with fractal heterogeneities, it reduces both the peak slip rate and the recurrence interval of the system-size earthquakes compared to a model with a lower rigidity in the entire bulk ($\mu = 20$ GPa; Fig. S3), as reported by Kaneko, Ampuero, and Lapusta (2011). However, the low-rigidity zone model still exhibits periodic cycles and does not introduce variability in hypocenter depth. Based on these results and given that reduced rigidity decreases the critical nucleation size (L_∞, Eq. (1) above), requiring higher numerical resolution, we chose not to include a fault zone in our reference unperturbed models.

References

Ampuero, J.-P., & Rubin, A. M. (2008). Earthquake nucleation on rate and state faults – Aging and slip laws. *Journal of Geophysical Research: Solid Earth*, *113*(B1).

Chester, F. M., Evans, J. P., & Biegel, R. L. (1993). Internal structure and weakening mechanisms of the San Andreas fault. *Journal of Geophysical Research: Solid Earth*, *98*(B1), 771–786.

Day, S. M., Dalguer, L. A., Lapusta, N., & Liu, Y. (2005). Comparison of finite difference and boundary integral solutions to three-dimensional spontaneous rupture. *Journal of Geophysical Research: Solid Earth*, *110*(B12).

Dieterich, J. H. (1992). Earthquake nucleation on faults with rate-and state-dependent strength. *Tectonophysics*, *211*(1-4), 115–134.

Dieterich, J. H. (1994). A constitutive law for rate of earthquake production and its application to earthquake clustering. *Journal of Geophysical Research: Solid Earth*, *99*(B2), 2601–2618.

Erickson, B. A., Jiang, J., Barall, M., Lapusta, N., Dunham, E. M., Harris, R., ... others (2020). The community code verification exercise for simulating sequences of earthquakes and aseismic slip (SEAS). *Seismological Research Letters*, *91*(2A), 874–890.

Huang, Y., Ampuero, J.-P., & Helmberger, D. V. (2014). Earthquake ruptures modulated by waves in damaged fault zones. *Journal of Geophysical Research: Solid Earth*, *119*(4), 3133–3154.

Idini, B., & Ampuero, J.-P. (2020). Fault-zone damage promotes pulse-like rupture and back-propagating fronts via quasi-static effects. *Geophysical Research Letters*, *47*(23), e2020GL090736.

Jiang, J., Erickson, B. A., Lambert, V. R., Ampuero, J.-P., Ando, R., Barbot, S. D., ... others (2022). Community-driven code comparisons for three-dimensional dynamic modeling of sequences of earthquakes and aseismic slip. *Journal of Geophysical Research: Solid Earth*, *127*(3), e2021JB023519.

Kaneko, Y., Ampuero, J.-P., & Lapusta, N. (2011). Spectral-element simulations of long-term fault slip: Effect of low-rigidity layers on earthquake-cycle dynamics. *Journal of Geophysical Research: Solid Earth*, *116*(B10).

Rice, J. R. (1993). Spatio-temporal complexity of slip on a fault. *Journal of Geophysical Research: Solid Earth*, *98*(B6), 9885–9907.

Rice, J. R., & Ben-Zion, Y. (1996). Slip complexity in earthquake fault models. *Proceedings of the National Academy of Sciences*, *93*(9), 3811–3818.

Rubin, A. M., & Ampuero, J.-P. (2005). Earthquake nucleation on (aging) rate and state faults. *Journal of Geophysical Research: Solid Earth*, *110*(B11).

Thakur, P., Huang, Y., & Kaneko, Y. (2020). Effects of low-velocity fault damage zones on long-term earthquake behaviors on mature strike-slip faults. *Journal of Geophysical Research: Solid Earth*, *125*(8), e2020JB019587.

Uphoff, C., May, D. A., & Gabriel, A.-A. (2023). A discontinuous Galerkin method for sequences of earthquakes and aseismic slip on multiple faults using unstructured curvilinear grids. *Geophysical Journal International*, *233*(1), 586–626.

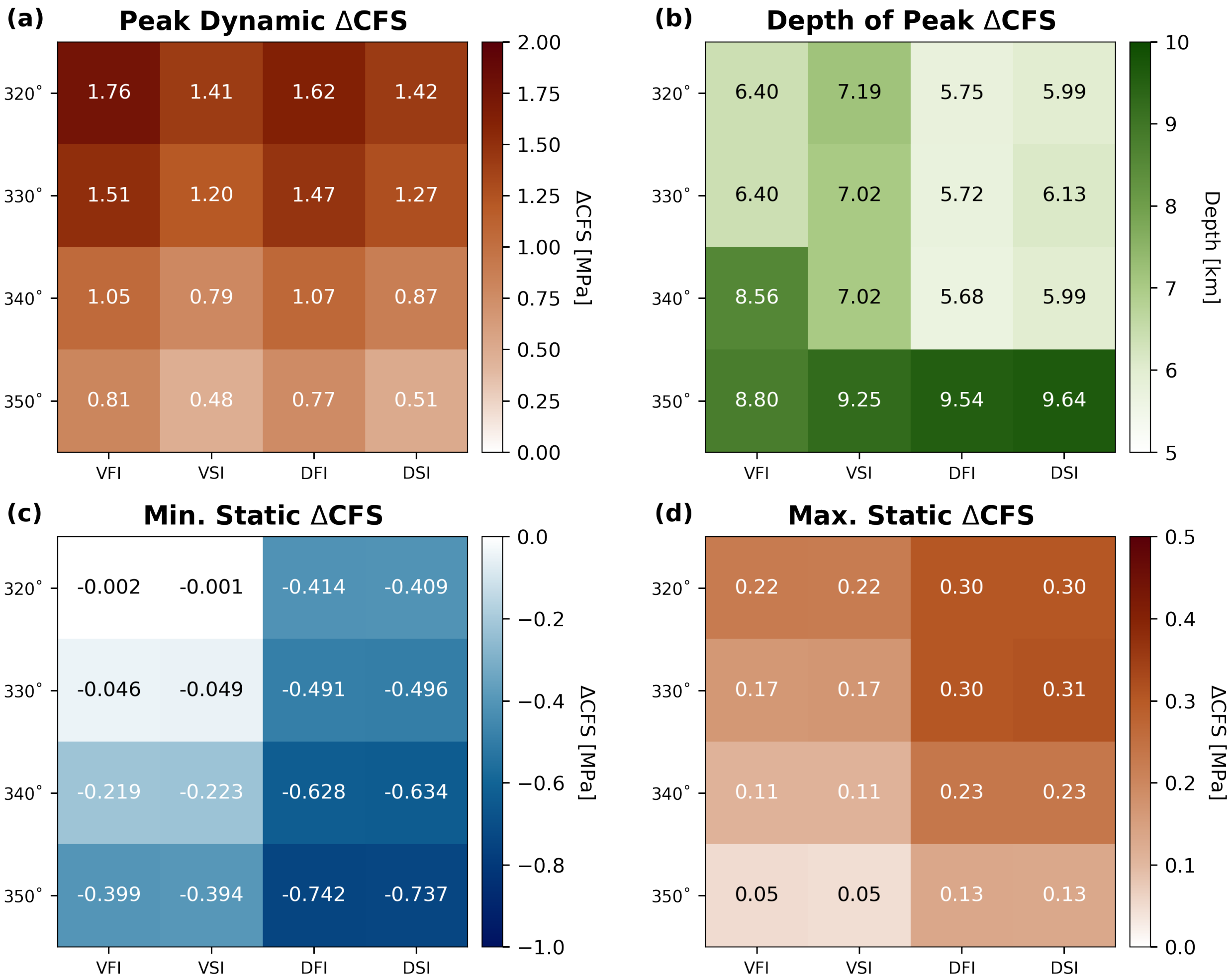

Figure S1. Summary of key values obtained from all 3D dynamic rupture models: (a) peak dynamic ΔCFS , (b) depth corresponding to the peak dynamic ΔCFS , (c) minimum static ΔCFS and (d) maximum static ΔCFS . (VFI: vertical foreshock fault, fast initiation; VSI: vertical foreshock fault, slow initiation; DFI: dipping foreshock fault, fast initiation; DSI: dipping foreshock fault, slow initiation.)

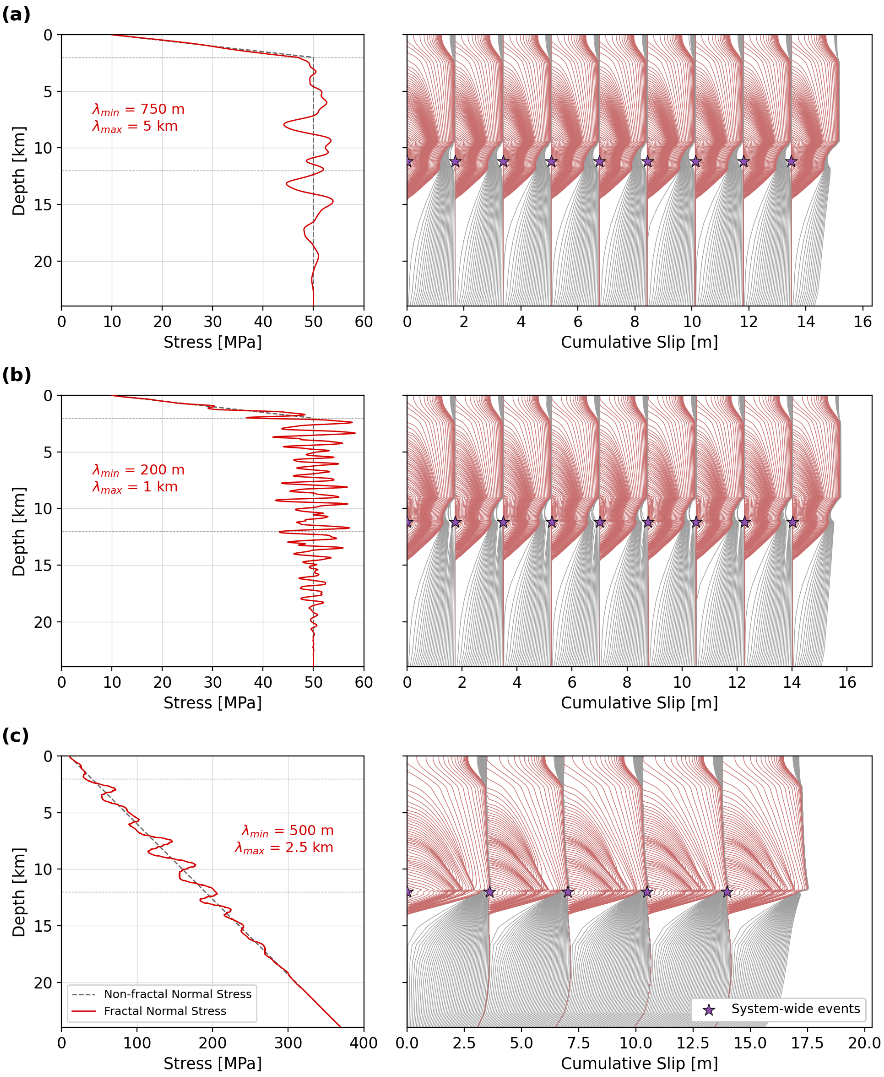

Figure S2. Seismic cycle models with heterogeneity only in initial effective normal stress. (a-b) Seismic cycle models with fractal heterogeneity using different limiting wavelengths of the fractal distribution (λ_{min} and λ_{max}, see Section 2.2.3 in the main text): (a) $\lambda_{min} = 750$ m and $\lambda_{max} = 5$ km, (b) $\lambda_{min} = 200$ m and $\lambda_{max} = 1$ km. (c) Seismic cycle model in which normal stress increases with depth with superimposed fractal heterogeneity ($\lambda_{min} = 500$ m and $\lambda_{max} = 2.5$ km). The left columns show the fractal distribution of the initial effective normal stress and the right columns show the corresponding cumulative slip evolution along the fault. Compare these with Figures 2b and 5a in the main text. All models show the cumulative slip omitting the first 200 years of spin-up time. The color scheme and marker usage are identical to those in Figure 5 in the main text.

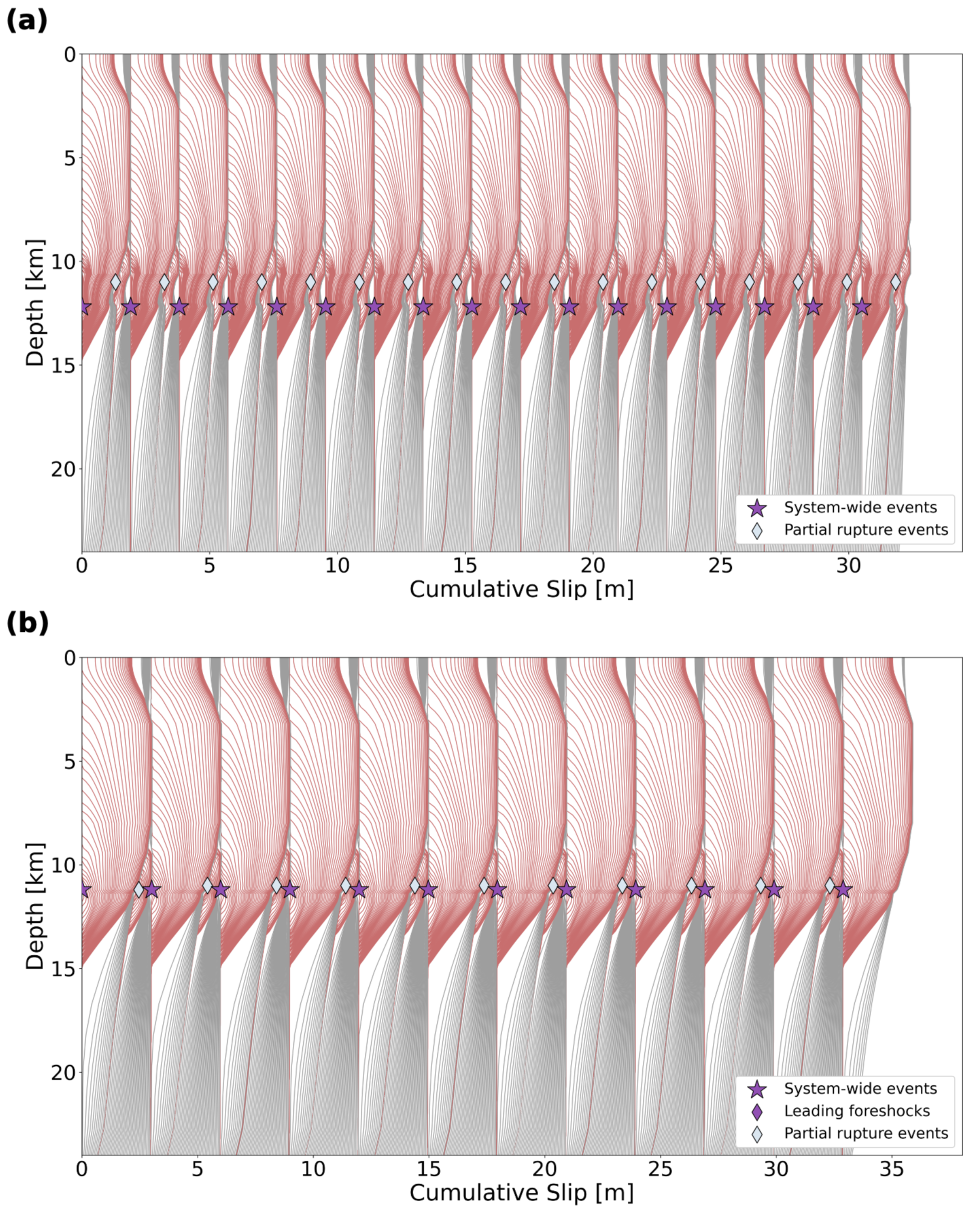

Figure S3. Comparison of seismic cycle models with and without a low-rigidity fault zone surrounding the fault (red shaded area in Fig. 2a in the main text). (a) Seismic cycle model with the low-rigidity fault zone ($\mu_{DZ} = 20$ GPa) embedded in the bulk with $\mu = 32$ GPa. (b) Seismic cycle model with a lower-rigidity bulk with $\mu = 20$ GPa. Both models share fractal heterogeneities in the initial effective normal stress and characteristic state evolution distance shown in Figures 2b and 2d in the main text. All models show the cumulative slip omitting the first 200 years of spin-up time. The color scheme and marker usage are identical to those in Figure 5 in the main text.

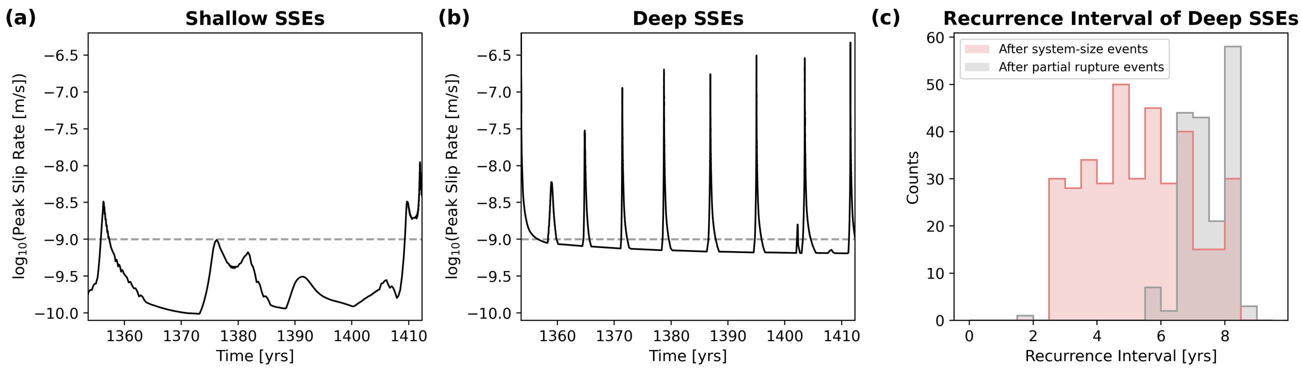

Figure S4. ESSEs in the reference aging law seismic cycle model. (a-b) Peak slip rate of the shallow (< 5 km) SSEs and the deep (10 km - 20 km) SSEs. The grey dashed line indicates the constant loading rate (V_{pl}). (c) Recurrence interval of the deep SSEs following system-size earthquakes (pink) and partial rupture events (grey).

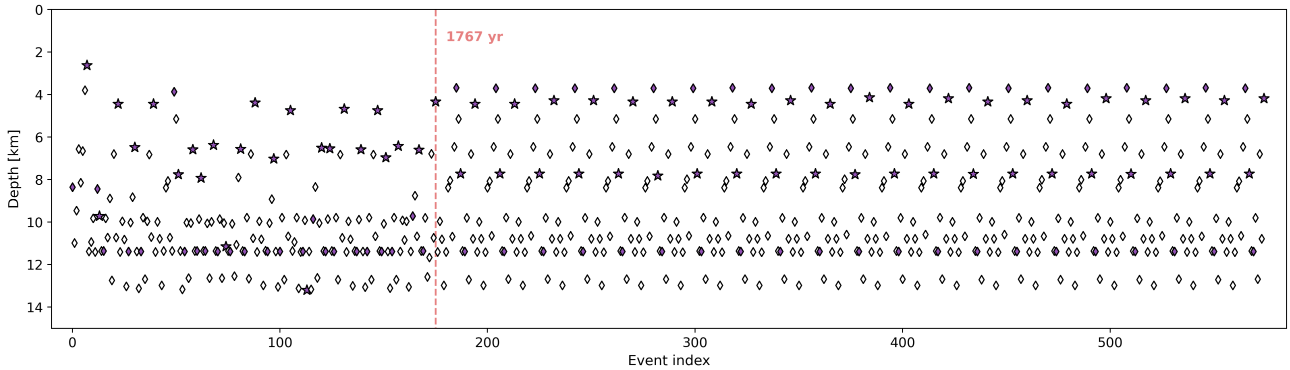

Figure S5. Hypocenter depth distribution for all earthquakes in the reference aging law seismic cycle model. A transition from an aperiodic to a quasi-periodic regime occurs after ∼1750 years of simulation time (pink dashed line). Purple stars, purple diamonds, and white diamonds indicate the hypocenter locations of system-size earthquakes, leading foreshocks, and partial rupture events, respectively.

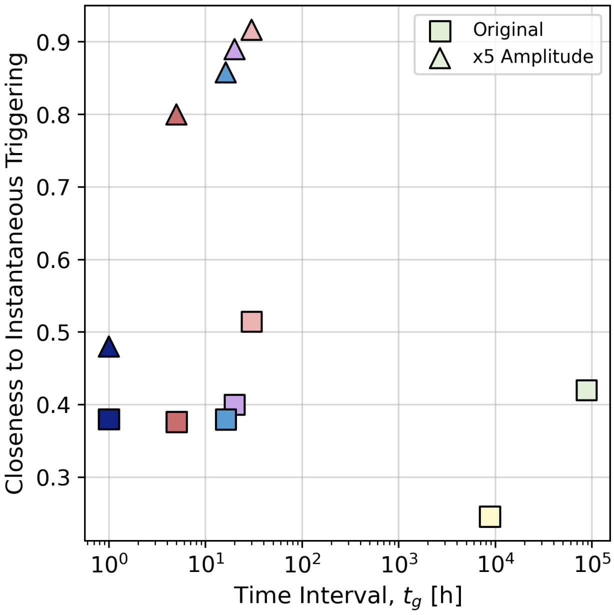

Figure S6. Closeness to instantaneous triggering (see Section 3.3 in the main text) for different perturbation timings (t_g). The squares represent the same seismic cycle simulations shown in Figure 8 in the main text while the triangles represent the seismic cycle simulations perturbing the same target event with 5-times amplified stress perturbation. The color scheme is identical to that in Figure 8 in the main text.)

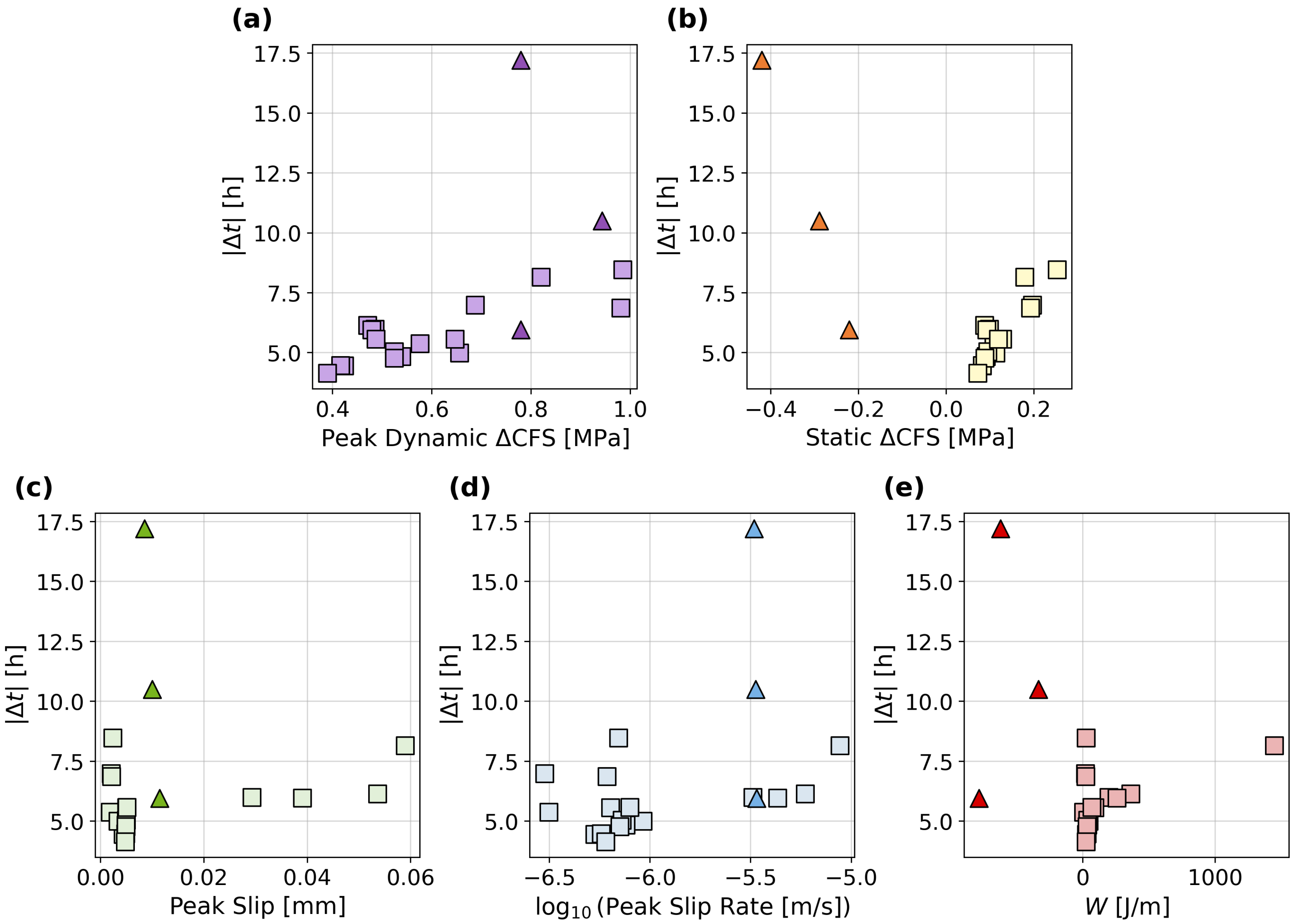

Figure S7. Same as Figure 7 in the main text (squares), but including clock delay models (triangles). For clarity, the absolute value of the mainshock clock change ($|\Delta t|$) is shown in the y-axis. A clear distinction between the clock advance models (squares) and the clock delay models (triangles) is observed in static ΔCFS (panel b) and work per distance, W (panel e).

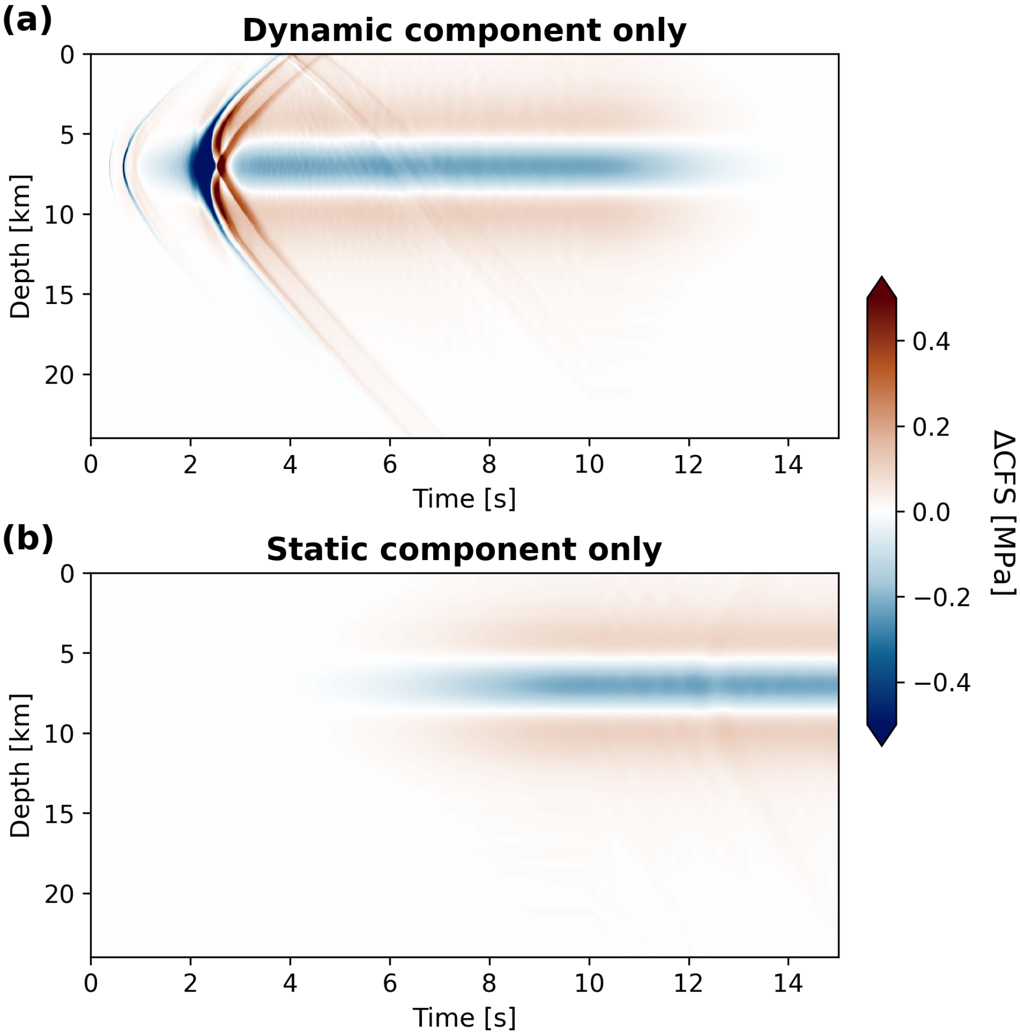

Figure S8. Spatiotemporal evolution of ΔCFS along the mainshock fault in 3D dynamic rupture models for models with (a) only the dynamic component of ΔCFS and (b) only the static component of ΔCFS . Panels (a) and (b) are utilized to generate perturbed seismic cycle models shown in Figures 11a and 11b in the main text, respectively.

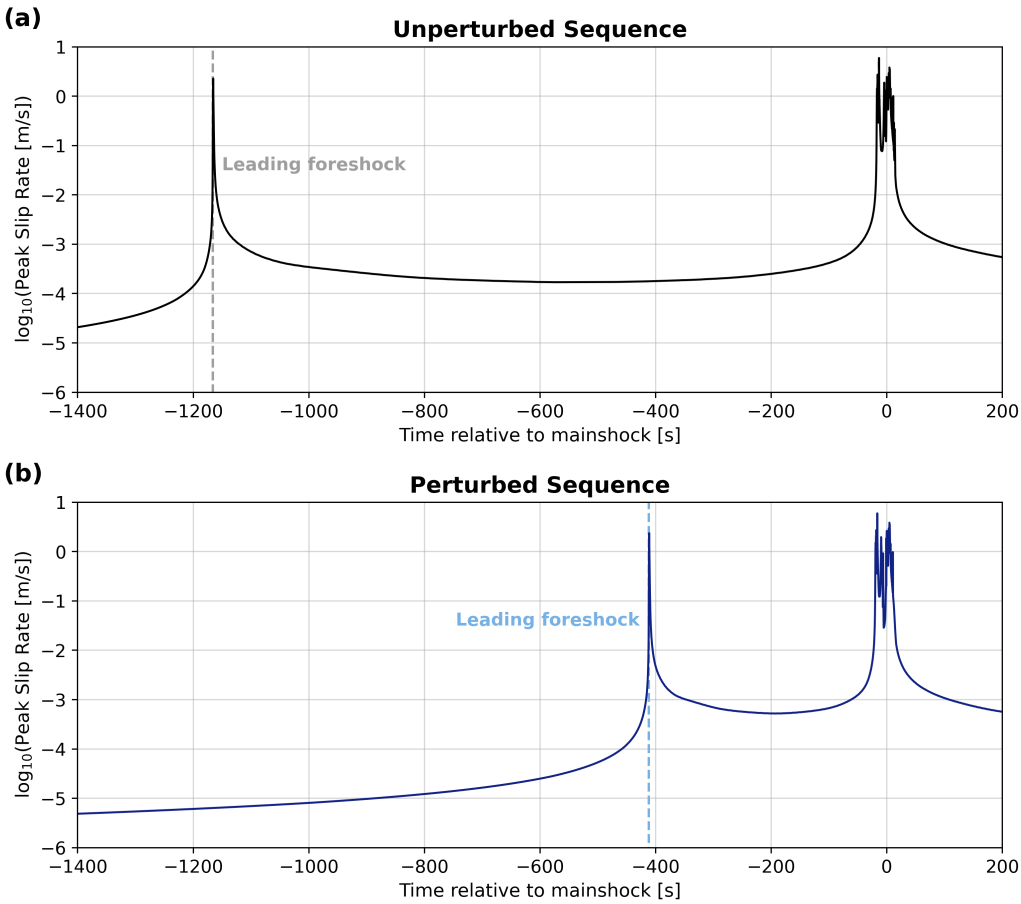

Figure S9. Shortening of the duration of the cascading foreshock-mainshock sequence in the seismic cycle model. Peak slip rate evolution of (a) the unperturbed model and (b) the perturbed model. The time from the leading foreshock (dashed lines) to the mainshock (zero in x-axis) reduces from 1166 seconds in the unperturbed sequence (a) to 411 seconds in the perturbed sequence (b). This example is generated by perturbing the reference aging law seismic cycle model using the stress perturbation from the dynamic rupture model with the vertical foreshock fault, slow initiation (VSI) with 340° strike orientation of the mainshock fault.

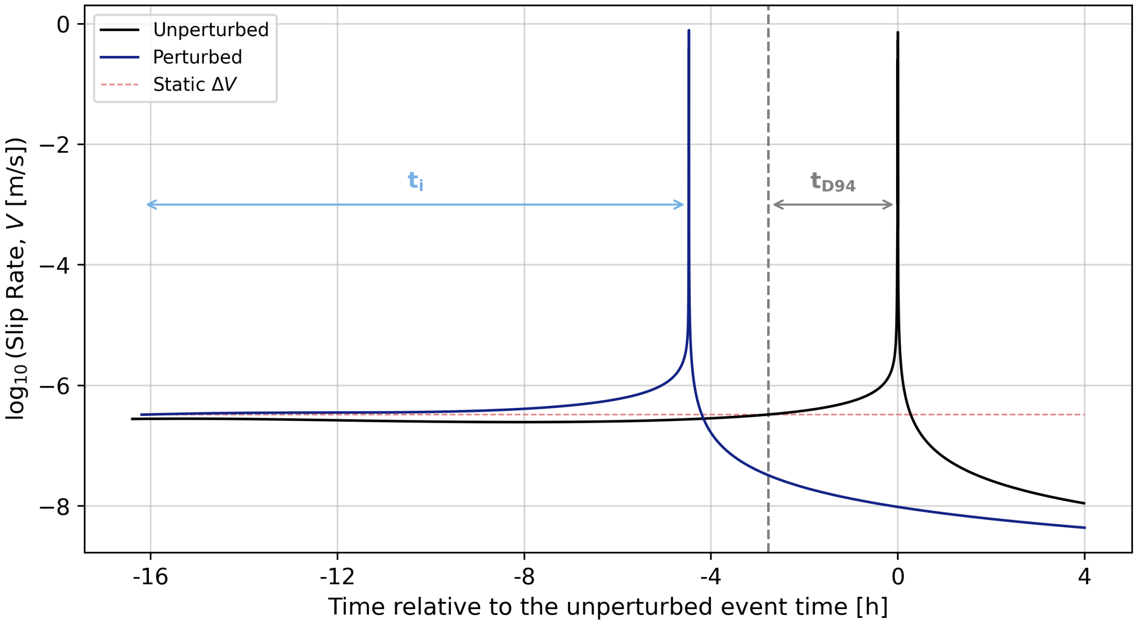

Figure S10. Comparison of time to instability measured from our seismic cycle simulation (t_i, blue arrow) to that predicted from a 1D spring-slider solution (t_{D94}, grey arrow; Dieterich, 1994). Slip rate evolution of the unperturbed model (black) and the perturbed model (dark blue) is obtained at a depth corresponding to the maximum aseismic slip during the perturbation period in each simulation ($z_{max} = 3.44$ km). The pink dotted line shows the quasi-constant increase in slip rate due to the perturbation and the grey dashed line marks the time when the slip rate in the unperturbed model reaches the increased slip rate.

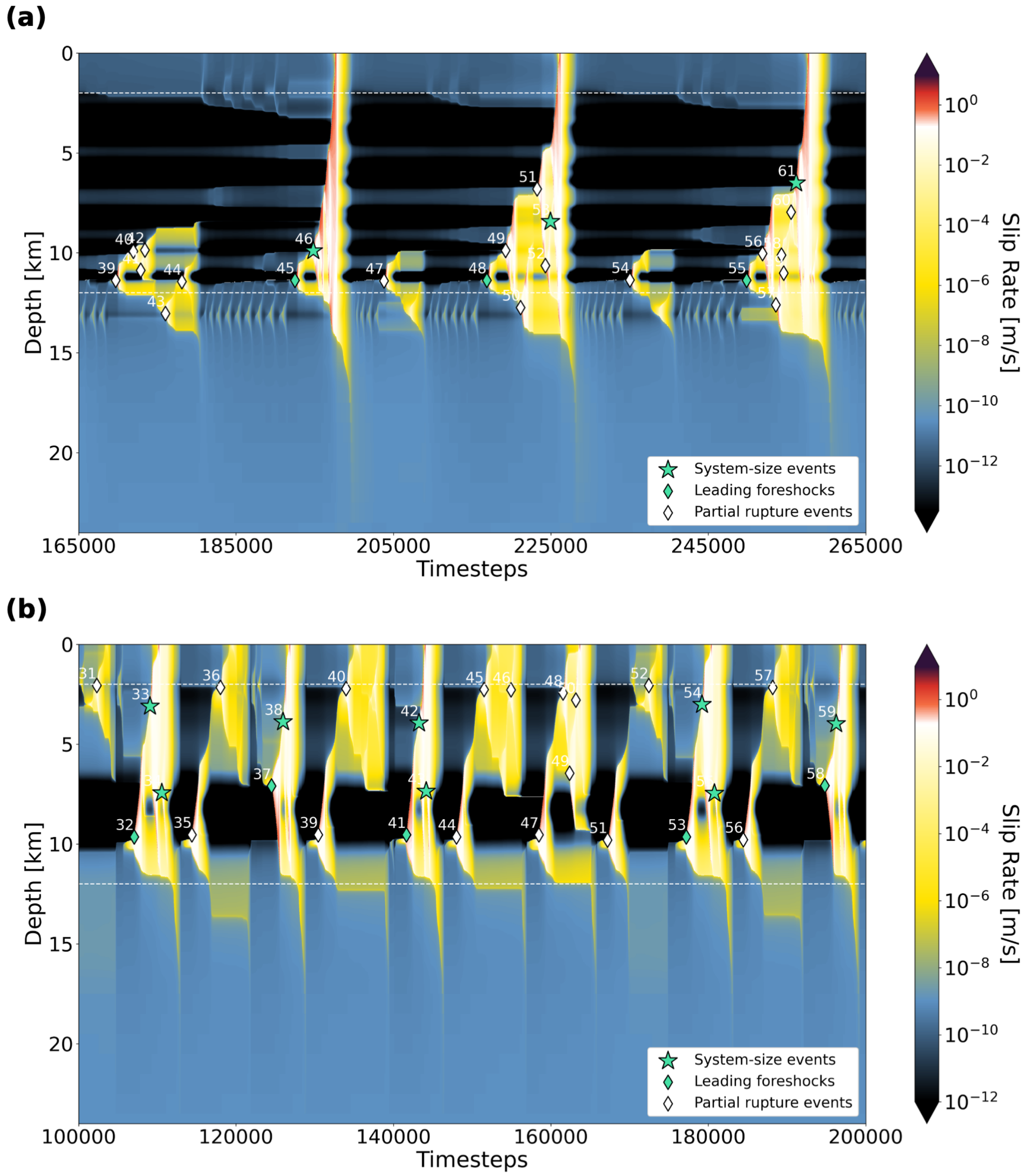

Figure S11. Spatiotemporal evolution of slip rate for seismic cycle models with different parameterization. (a) Seismic cycle model with $V_{pl} = 3.2\times10^{-11}$ m/s, showing the period between 11520 years and 19880 years of simulation time. (b) Seismic cycle model with fractal heterogeneity in all three parameters using limiting bandwidths of $\lambda_{min} = 30$ m and $\lambda_{max} = 10$ km, showing the period between 338 years and 710 years of simulation time. The color scheme and marker usage are identical to those in Figure 6 in the main text.

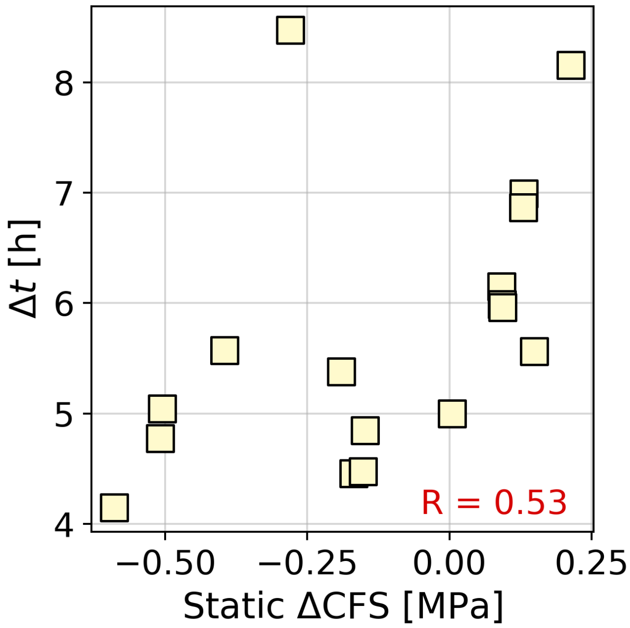

Figure S12. Same as Figure 7b in the main text, but measured at the target hypocenter depth in each unperturbed model. Note the cases where static ΔCFS values are negative but resulting in mainshock clock advances (i.e., $\Delta t > 0$).

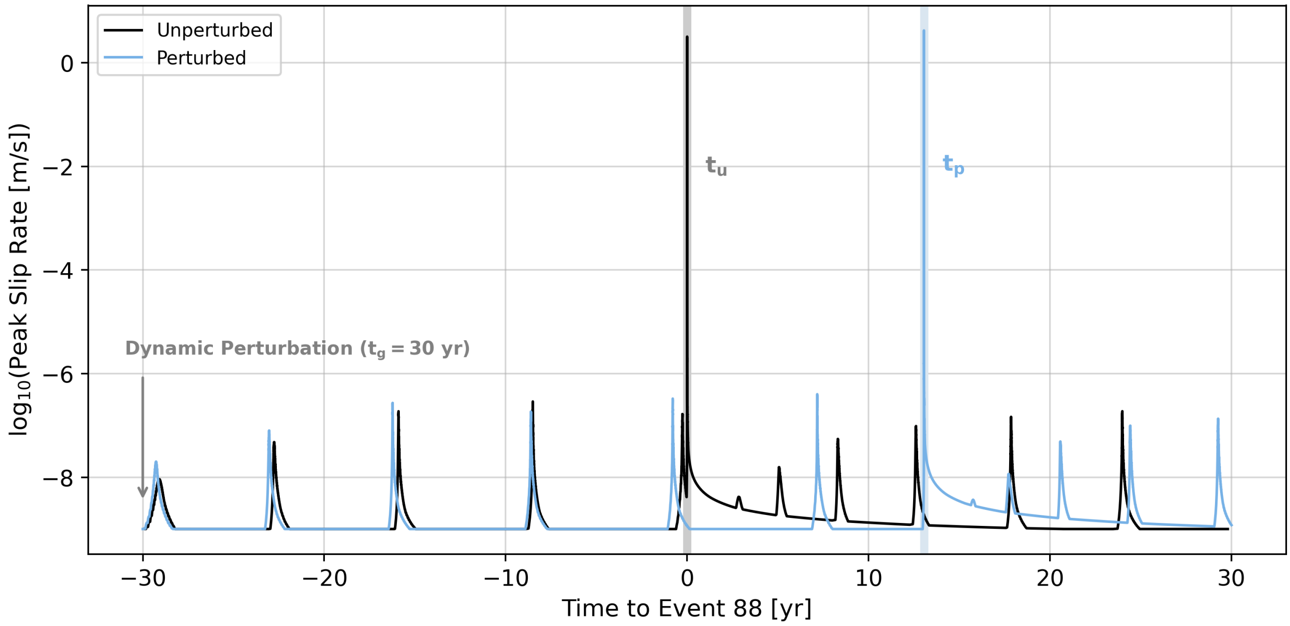

Figure S13. Peak slip rate of the unperturbed model (black) and perturbed model (blue) when $t_g = 30$ years (grey arrow), showing $\sim$ 13 years delay of the mainshock. The example simulation shown here is identical to that in Figure 8 in the main text.

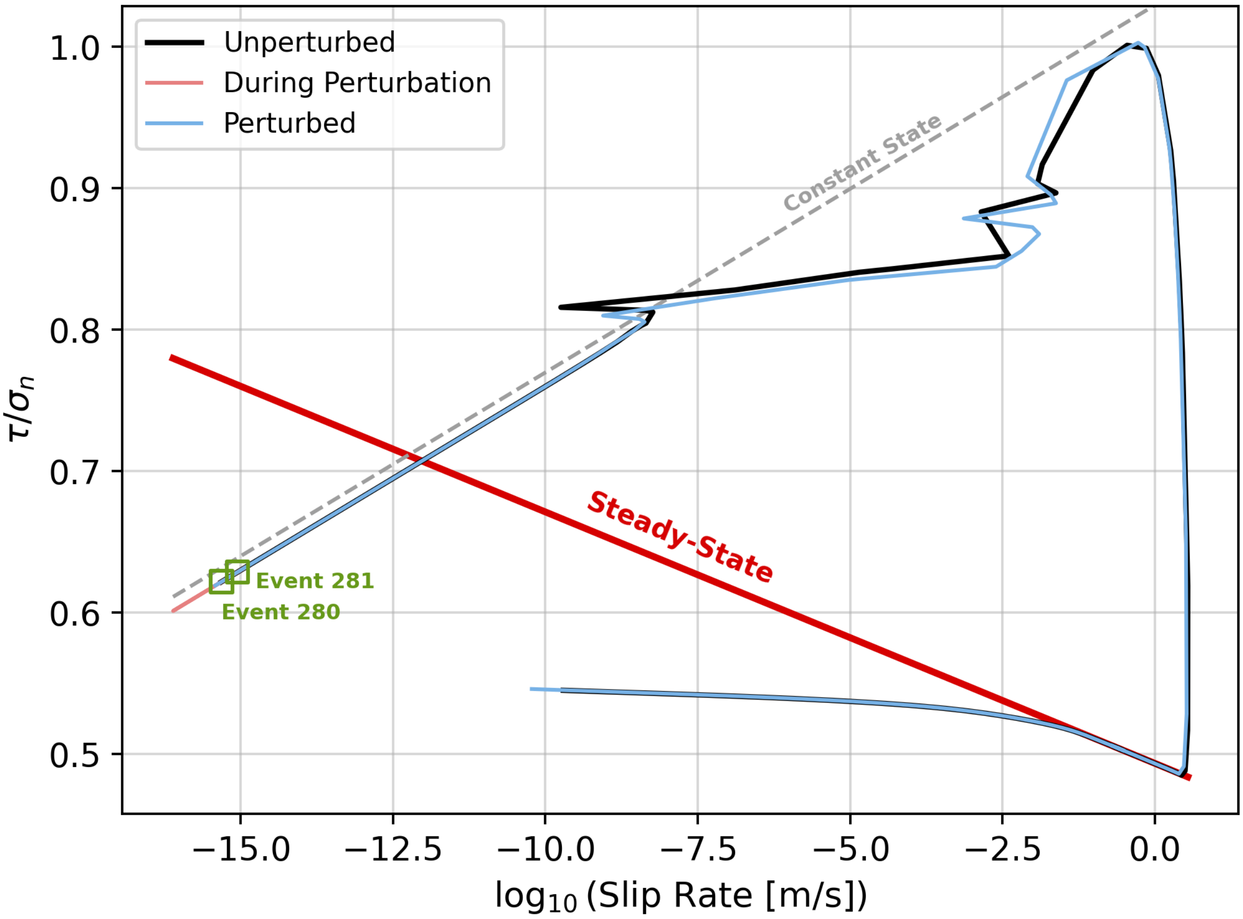

Figure S14. Same as Figure 13 in the main text, but measured at the hypocenter depth in the unperturbed model (7.82 km). Green boxes mark the two foreshocks preceding the mainshock.

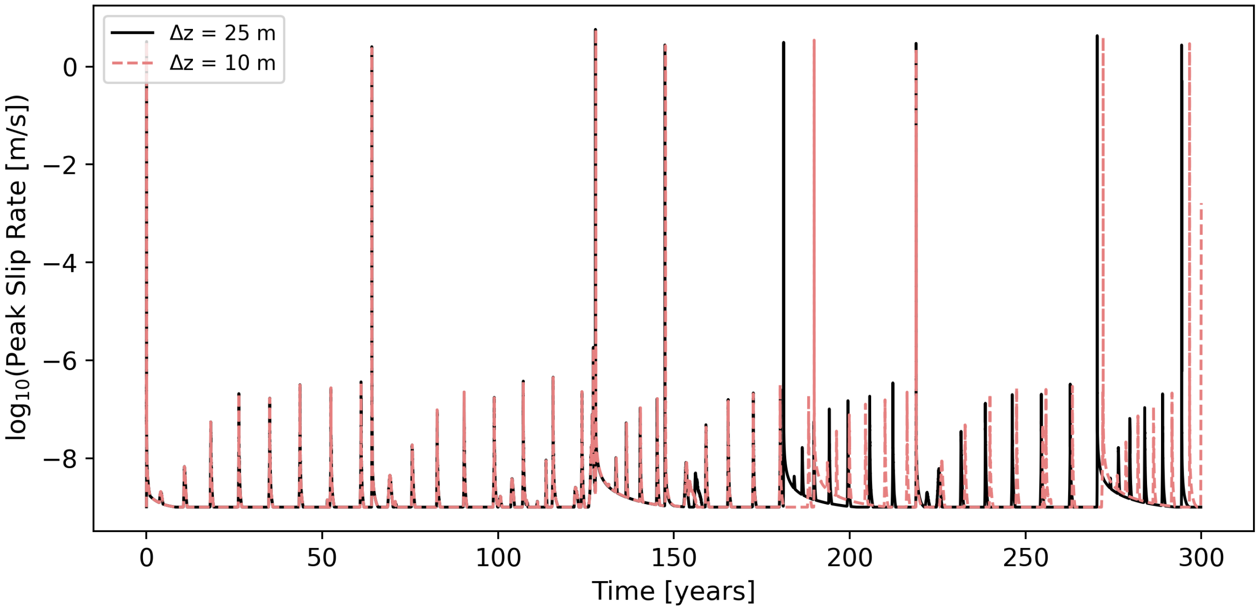

Figure S15. Peak slip rate evolution of reference aging law seismic cycle models with $\Delta z =$ 25 m (black solid line) and $\Delta z =$ 10 m (pink dashed line). The two models agree well before $\sim$ 150 years.